RSC Advances

PAPER

View Article Online
View Journal | View Issue

Cite this: *RSC Adv.*, 2025, **15**, 43702

Deep insights into lead-free Sr_3BiI_3-based anti-perovskite solar cells: optimization strategies and impedance spectroscopy *via* numerical simulation and machine learning

Bipul Chandra Biswas,[a] Karim Kriaa,[b] Asadul Islam Shimul,[a] Chemseddine Maatki,[b] Md. Azizur Rahman *[c] and Noureddine Elboughdir[d]

Anti-perovskite solar cells (APSCs) are garnering substantial attention due to their promising potential in the renewable energy sector and their distinctive characteristics. This research investigates the structural, optical, and electrical properties of Sr_3BiI_3 using Density Functional Theory (DFT) and further evaluates its photovoltaic (PV) performance in Sr_3BiI_3-based lead-free APSCs through the SCAPS-1D simulator. The device architectures employ Sr_3BiI_3 absorbers and explore the impact of different electron transport layers (ETLs) including WS_2, IGZO, PCBM, and SnS_2, alongside with the multiple hole transport layer (HTL). The impacts of layer thickness, defect density, doping concentration, series and shunt resistances, operating temperature, and impedance response (evaluated through Nyquist plots) are systematically examined for all ETLs. The power conversion efficiency (PCE) of devices optimized with WS_2, IGZO, PCBM, and SnS_2 as ETL and CBTS as HTL were determined to be 30.20%, 30.12%, 29.18%, and 30.31%, respectively. To further improve device optimization, machine learning models, particularly Random Forest, were trained on SCAPS-1D simulation results. The application of machine learning models reduces experimental duration and eliminates the need for extensive resources in the design and prediction of PV performance in solar cells. The model forecasts performance with an impressive correlation coefficient (R^2) of 0.989 for PCE. To enhance interpretability, methods such as correlation heatmaps, feature importance, and SHAP analysis were employed to assess the impact of critical parameters on device efficiency. The suggested framework provides a reliable and efficient method for forecasting the most significant factors and their influence on the performance of Sr_3BiI_3-based APSCs.

Received 25th September 2025
Accepted 27th October 2025

DOI: 10.1039/d5ra07289a

rsc.li/rsc-advances

1. Introduction

The increasing focus on solar energy highlights the essential role of renewable resources in the enduring sustainability and progress of human civilization. Within the solar energy sector, perovskite solar cells (PSCs), have emerged as a key technology, with efficiencies of up to 27% in single-junction designs.[1] This exceptional performance establishes PSCs as formidable rivals to conventional silicon solar cells (SCs). Equally remarkable is their swift advancement toward commercialization, a milestone that has attained slightly over a decade from their establishment. The extensive industrial use of PSCs is impeded by various problems, including the devices' stability under light exposure in ambient circumstances and the toxicity of its constituent elements.[2,3]

Anti-perovskite-derived materials are often defined by the crystal structure A_3BX_3, in which "A" and "B" signify big and tiny metallic cations, respectively, and "X" represents a halogen anion.[4] Recently, significant focus has been placed on lead-free A_3BX_3 perovskites owing to their remarkable characteristics. These materials have a direct bandgap, which is particularly beneficial for optoelectronic applications.[5] Their exceptional light absorption and mechanical resilience render them suitable for several applications. Lead-free perovskites demonstrate exceptional optical characteristics, including a high dielectric constant, a notable refractive index, and robust optical conductivity, positioning them as viable choices for sustainable and efficient optoelectronic devices.[6,7] Strontium-based anti-perovskites, exemplified by Sr_3BiI_3, have drawn interest as potentially useful materials for SC applications.[8] Their cubic crystal structure promotes advantageous band edge transitions, improving their optical characteristics and making them appropriate for industrial applications. The structural

[a]*Department of Electrical and Electronic Engineering, Gopalganj Science and Technology University, Gopalganj-8100, Bangladesh*
[b]*Imam Mohammad Ibn Saud Islamic University (IMSIU), Riyadh 11432, Saudi Arabia*
[c]*Department of Electrical and Electronic Engineering, Begum Rokeya University, Rangpur 5400, Bangladesh. E-mail: azizurrahmanatik49@gmail.com*
[d]*Chemical Engineering Department, College of Engineering, University of Ha'il, P. O. Box 2440, Ha'il 81441, Saudi Arabia*

resemblance of Sr_3BX_3 (with B = Sb, Bi, As; X = halides) to halide anti-perovskites enhances light absorption, thus augmenting photovoltaic (PV) efficiency.[9] Despite its toxicity with arsenic, like lead, it is nevertheless employed in many technologies such as SCs, detectors, and superconductors due to its exceptional performance. GaAs-based SCs are recognized for their effective encapsulation methods that reduce the dangers of hazardous material leakage.[10] Bismuth-containing double perovskites, exemplified as A_2AgBiX_6 (where A = K, Cs, Rb and X = Cl, I, Br), are increasingly acknowledged for their promise in optoelectronic applications and solar energy systems.[11,12] In this context, strontium bismuth halides, specifically Sr_3BiI_3, have emerged as promising lead-free anti-perovskite materials that integrate environmental safety with superior optoelectronic performance. Structurally, Sr_3BiI_3 crystallizes in a distorted anti-perovskite-related lattice, wherein the integration of Bi^{3+} ions into the Sr–I framework augments lattice stability, reduces defect formation, and produces a direct band gap of 1.1–1.2 eV, optimally suited for solar energy absorption. Furthermore, its tolerance factor (~0.96) guarantees a stable cubic anti-perovskite phase that is impervious to phase segregation and structural distortion.[13–15] The robust Bi–I covalency facilitates shallow defect states and diminishes nonradiative recombination, whereas the compatible ionic radii of Sr^{2+} and Bi^{3+} enhance structural uniformity and oxidation resistance successfully addressing the inherent instability that constrains Sn-based anti-perovskites.[16,17] From an electronic standpoint, Sr_3BiI_3 exhibits advantageous band alignment with commonly utilized transport materials: its conduction band aligns effectively with WS_2, IGZO, and SnS_2 as ETLs, while its valence band corresponds suitably with CBTS and NiO as HTLs. This alignment facilitates balanced charge extraction, diminishes interfacial recombination, and improves overall device efficiency.[18] Moreover, the material's reduced exciton binding energy and elevated thermal stability promote effective carrier separation and extended operational longevity under light.[19] The features of chemical durability, improved band structure, and environmental compatibility provide Sr_3BiI_3 an attractive and sustainable absorber for next-generation lead-free APSCs.

Numerous studies have examined strontium-based anti-perovskites owing to their advantageous optoelectronic and structural characteristics, rendering them viable candidates for high-efficiency and environmentally friendly solar cell applications. Rahman *et al.*[20] utilized SCAPS-1D simulations to investigate the inorganic Sr_3NCl_3-based PSC, revealing its significant potential for solar energy application due to its direct band gap of 1.649 eV, superior optical absorption, and strong crystalline stability, all of which enhance PV performance. In a separate investigation, the device configuration of FTO/ZnO/Sr_3PCl_3/Cu_2O/Ni demonstrated remarkable PV performance, featuring an FF of 89.9%, a V_{OC} of 1.3 V, a J_{SC} of 22.79 mA cm^{-2}, and a PCE of 26.67%, underscoring the significant potential of strontium-based compounds for solar energy conversion.[21] Additionally, Ghosh *et al.*[22] used SnS_2 as ETL with Sr_3PI_3, attaining a PCE of 27.32%. The Sr_3PI_3 material exhibited superior dielectric characteristics and notable absorption peaks within the solar photon energy spectrum, affirming its appropriateness as a non-toxic, high-performance material for semiconductor and solar cell applications.[23] Building on this basis, Sr_3BiI_3 has lately emerged as a notably promising lead-free anti-perovskite due to its ductility, elevated dielectric constant, and exceptional electrical conductivity, which together improves charge transfer and diminishes recombination losses. In comparison to other lead-free options such $Cs_3Sb_2I_9$, $FASnI_3$, $MASnI_3$, and $MASnBr_3$, Sr_3BiI_3 exhibits a more equitable compromise among efficiency, stability, and environmental safety.[24–26] Despite $Cs_3Sb_2I_9$ being entirely non-toxic and chemically stable, its indirect band gap (~2.0 eV) and low-dimensional layered architecture hinder carrier transport and restrict light absorption, leading to diminished power conversion efficiencies and inconsistent performance.[27] Conversely, Sn-based perovskites like $FASnI_3$ $MASnI_3$, and $MASnBr_3$ have direct band gaps (1.3–1.5 eV) and significant absorption; yet their instability resulting from Sn^{2+} oxidation to Sn^{4+} induces trap state formation, non-radiative recombination, and swift deterioration in ambient circumstances.[28] Conversely, Sr_3BiI_3 demonstrates structural and thermal stability, an almost optimum direct band gap (~1.74 eV), and exceptional environmental durability, while circumventing the oxidation-induced instability characteristic of Sn-based perovskites. The inherent benefits position Sr_3BiI_3 as a next-generation lead-free anti-perovskite absorber, effectively reconciling efficiency, stability, and sustainability, thereby facilitating the development of durable, high-efficiency, and environmentally friendly APSCs.

This study presents a comprehensive analysis of the optoelectronic properties of Sr_3BiI_3 using DFT, highlighting its potential as anti-perovskite absorber layer to optimize device configurations and enhance efficiency. The objective is to attain optimal efficiency by integrating HTL with diverse ETLs including WS_2, IGZO, PCBM, and SnS_2, utilizing SCAPS-1D software. The primary focus of this research is to investigate the potential for performance improvement with Sr_3BiI_3-based APSCs, as there is a lack of research on this material. Four unique device topologies using various ETL combinations were examined to enhance the efficiency of Sr_3BiI_3-based APSCs. The research further examines the influence of ETLs on band alignment, thickness, defect density, doping density, interface defects, series and shunt resistance (R_s and R_{Sh}), quantum efficiency (QE), operating temperature, and current–voltage (J–V) behavior. The results validate the potential of Sr_3BiI_3-based APSCs as a viable option for next-generation PV technology.

2. Computational specifications

2.1. DFT and SCAPS 1D

This study employed first-principles calculations grounded in DFT with the CASTEP module of the Materials Studio 2017 package[29] to examine the mechanical, structural, electrical, and optical aspects of the Sr_3BiI_3 anti-perovskite. The initial cubic unit cell of Sr_3BiI_3 was created and displayed with VESTA software,[30] and this optimized structure provided the basis for all subsequent simulations. The Generalized Gradient Approximation (GGA) utilizing the Perdew–Burke–Ernzerhof (PBE) functional was utilized for the treatment of exchange–

correlation interactions. The Koelling–Harmon relativistic method, in conjunction with Vanderbilt's ultrasoft pseudopotentials (USP), was utilized to precisely characterize the electron–ion interactions. Structural relaxations were accomplished *via* the Broyden–Fletcher–Goldfarb–Shanno (BFGS) reduction method until convergence in energy, force, and stress was attained.[31] The plane-wave cutoff energy was established at 350 eV, and Brillouin zone sampling was performed utilizing a $10 \times 10 \times 10$ Monkhorst–Pack k-point mesh to guarantee well-converged outcomes. The convergence criteria for atomic relaxation in CASTEP comprised a total energy tolerance of 2×10^{-5} eV per atom, a maximum atomic movement of 5×10^{-4} Å, a maximum force of 0.05 eV $Å^{-1}$, and a stress threshold of 0.02 GPa. The elastic constants (C_{ij}) were obtained by the finite strain method, and their anisotropic variations were examined through 2D and 3D surface contour plots of elastic moduli produced with the ELATE software.[32] SCAPS-1D simulations were employed to model the device-level performance of Sr_3BiI_3-based APSCs.[33] This widely used one-dimensional device simulator solves Poisson's equation, charge continuity, and carrier transport equations, enabling the evaluation of carrier dynamics, recombination mechanisms, and transport properties under standard AM 1.5 illumination.[34,35] These simulations provided critical insights into band alignment at interfaces, carrier extraction efficiency, recombination kinetics, and defect-related limitations. Additionally, optimization evaluations regarding layer thickness, doping concentration, and defect density were performed to identify strategies for improving device performance. This integrated DFT and device-level modeling methodology enabled a comprehensive understanding of the intrinsic material characteristics and optoelectronic device performance of Sr_3BiI_3 anti-perovskite, laying the groundwork for its potential application in PVs and other optoelectronic technologies.

2.2. Machine learning

Machine learning techniques were utilized to forecast and optimize the PV performance of Sr_3BiI_3-based APSCs utilizing Python, selected for its versatility and comprehensive support in artificial intelligence and scientific computing.[36,37] The computational framework incorporated Pandas, NumPy, and Scikit-learn (v1.4) libraries within the Google Colab environment, facilitating quick data preprocessing, feature engineering, and model creation. Among the several regression algorithms analyzed, the Random Forest (RF) exhibited the most formidable predictive performance and resistance to overfitting, attributable to its ensemble architecture and capacity to capture intricate nonlinear relationships among PV parameters. The dataset, produced *via* SCAPS-1D simulations, methodically altered intrinsic and extrinsic parameters of the absorber and charge transport layers yielding a total of 13 986 data points. Of them, 80% (11 189 samples) were allocated for training, whilst 20% (2797 samples) were designated for model testing and validation. Ten principal material and device parameters were utilized as input features, encompassing absorber thickness, acceptor density, defect density, band gap, electron affinity, dielectric permittivity, electron and hole mobilities, interface defect density, and operating temperature. The target outputs included V_{OC}, J_{SC}, FF, and PCE. A systematic workflow was employed for model implementation, as outlined in Algorithm 1, encompassing environment initialization, dataset acquisition, data cleansing, imputation of missing values (mean for numerical and mode for categorical data), one-hot encoding of categorical variables, dataset partitioning (80 : 20), and feature standardization utilizing StandardScaler. The preprocessed dataset was utilized to train RFR model, and its predictive accuracy was assessed through various statistical metrics, including the coefficient of determination (R^2), Mean Absolute Error (MAE), Mean Squared Error (MSE), Root Mean Squared Error (RMSE), and Mean Absolute Percentage Error (MAPE). A two-fold cross-validation method was utilized to enhance robustness and generalization, hence reducing model bias and variation. The sequential execution is delineated as follows:

Algorithm 1: Execution of the proposed machine learning model.

Step 1: Establish the computational environment.

Step 2: Import the dataset generated by SCAPS.

Step 3: Address absent data by statistical imputation.

Step 4: Implement one-hot encoding for categorical variables.

Step 5: Divide the dataset into input features (X) and target variables (Y).

Step 6: Divide the dataset into 80% for training and 20% for testing groups.

Step 7: Standardize features utilizing StandardScaler.

Step 8: Train the model utilizing the Random Forest.

Step 9: Forecast target variables (V_{OC}, J_{SC}, FF, PCE).

Step 10: Assess the model utilizing R2, MAE, MSE, RMSE, and MAPE measures.

Step 11: Conclude following validation and performance evaluation.

This systematic methodology facilitated precise prediction and interpretability of device performance, while allowing for the discovery of critical physical parameters that influence the PV efficiency of Sr_3BiI_3-based APSCs.

3. Result and discussion

3.1. Examination of DFT result

3.1.1. Structural characteristics of the Sr_3BiI_3 compound. The structural properties of Sr_3BiI_3, classified under the cubic space group $Pm\bar{3}m$ (no. 221),[38] are illustrated in Fig. 1(a) and (b). The primary structural unit is the cubic unit cell, with a total of seven atoms. Each unit cell of three Sr atoms, one Bi atom, and three I atoms. The atomic configuration within the cell adheres to specific Wyckoff positions: Sr atoms are located at the 3c (0.5, 0.5, 0) sites, the P atom is situated at the 1b (0.5, 0.5, 0.5) site, and Br atoms are found at the 3d (0.5, 0, 0) sites. This atomic arrangement illustrates the very symmetrical structure of the cubic lattice.

The complete structural optimization revealed an equilibrium lattice constant of 6.845 Å, aligning well with previous

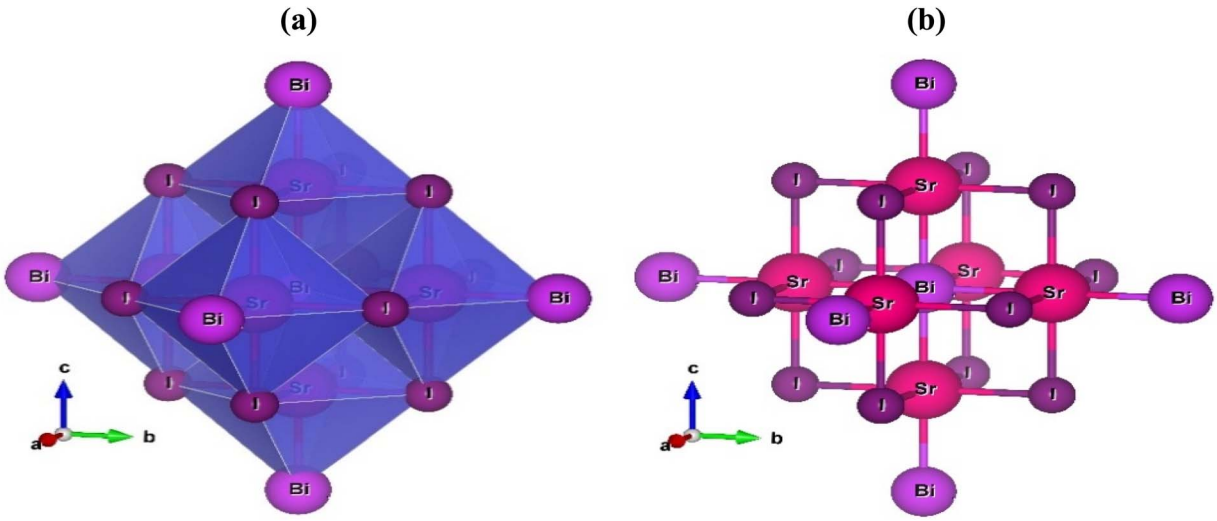

Fig. 1 The crystal structure of Sr_3BiI_3-based anti-perovskite-derived materials is shown in (a) polyhedral and (b) ball-and-stick models.

theoretical studies.[8,39] Optimized structural data offers a dependable basis for the subsequent investigation of the material's electrical and optical characteristics.

3.1.2. Band structure, density of states, and charge density of the Sr_3BiI_3 compound. The band structure of Sr_3BiI_3 was calculated to obtain a more profound understanding of its electrical features, as depicted in Fig. 2(a). The computed E-k diagram distinctly illustrates that at the Fermi level (E_F), there exists a clear demarcation between the valence band (occupied states) and the conduction band (unoccupied states), hence affirming the semiconducting characteristics of the material. The valence band maximum (VBM) and conduction band minimum (CBM) are situated at the identical high-symmetry point (Γ-point) in the Brillouin zone, confirming the existence of a straight band gap. The predicted band gap value of 1.164 eV is within the ideal range documented in the literature,[8,39] indicating that Sr_3BiI_3 is highly promising for PV and optoelectronic applications, where direct transitions facilitate effective light absorption. The current calculations exclude spin–orbit coupling (SOC) effects, which are significant for materials with heavy elements such as Bi. The absence of SOC in this study simplifies calculations and facilitates clearer insights into the intrinsic properties of Sr_3BiI_3, despite SOC expected influence on the band structure and optical properties. Without considering SOC effects, the model emphasizes primary electronic interactions, thereby eliminating complexities from spin interactions and facilitating the interpretation of the material's fundamental semiconducting behavior.

The density of states (DOS) analysis presented in Fig. 2(b) offers supplementary information. The valence band edge is mostly determined by I 4d orbitals, with slight contributions from Bi 5d states, whereas the conduction band edge is predominantly derived from Sr 3d orbitals, with lesser involvement of I 5p states. The overlapping orbital contributions suggest hybridization among the electronic states of Sr, Bi, and I, which is crucial for maintaining the crystal structure *via* robust bonding interactions. The electron charge density distribution of Sr_3BiI_3, examined along the (100) crystallographic plane, offers essential information into its bonding characteristics and electrical structure. The contour map (Fig. 2(c)) clearly delineates areas of electron concentration and depletion, with calcium atoms encircled by dense, spherical charge distributions. This symmetry indicates robust Sr–I ionic interactions, with minimal orbital overlap or electron

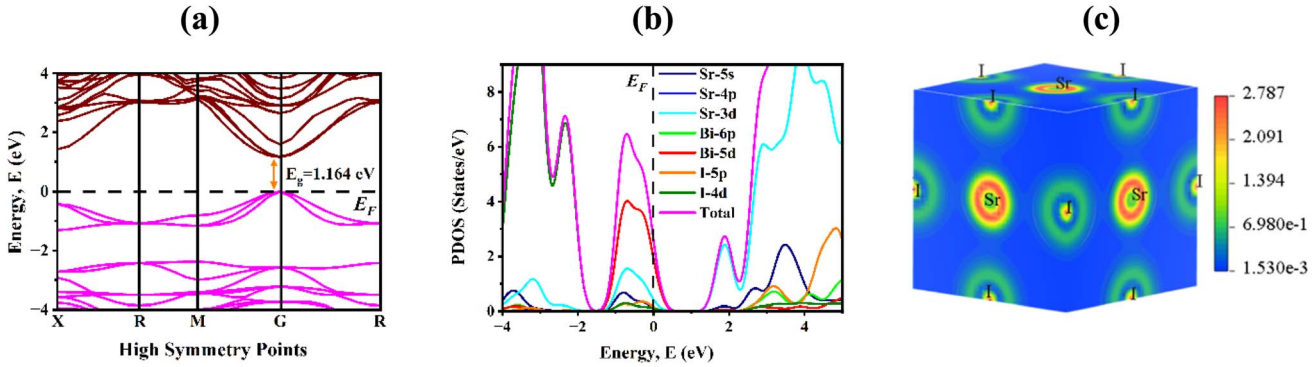

Fig. 2 Electronic properties of Sr_3BiI_3 anti-perovskite showing (a) band gap, (b) DOS, and (c) charge density distribution.

delocalization among Sr, Bi, and I atoms. These observations verify that the bonding structure is primarily ionic rather than covalent. The charge density is consistently distributed across the lattice, regardless of orientation, indicating the isotropic electrical nature of the material. This uniformity highlights the stability of the electrostatic environment, which is particularly beneficial for maintaining structural integrity. Moreover, the uniform charge distribution augments the applicability of Sr_3BiI_3 for functional uses, including solar energy absorbers, dielectric layers, and optoelectronic devices, where uniform electrical and structural characteristics are critical.

3.1.3. Optical characteristics of the Sr_3BiI_3 compound. The optical response of semiconducting materials is intrinsically connected to their electronic band structure, especially the forbidden energy gap, which is crucial for enhancing device performance. The capacity of a material to absorb photons in optoelectronic and PV applications is directly determined by its bandgap energy.[40] A comprehensive examination of the optical properties of Sr_3BiI_3 is crucial to evaluate its viability as a functional material, given that optical characteristics can be adjusted for certain purposes. A thorough analysis was conducted utilizing various frequency-dependent optical functions, such as the complex dielectric function, refractive index, reflectivity, optical conductivity, absorption coefficient, and energy loss function. The complex dielectric function $\varepsilon(\omega) = \varepsilon_1(\omega) + i\varepsilon_2(\omega)$ offers essential insights into the material's reaction to incoming electromagnetic (EM) radiation.[41] The real component, $\varepsilon_1(\omega)$, indicates the medium's capacity to store and transmit energy, whereas the imaginary component, $\varepsilon_2(\omega)$, signifies photon absorption and electronic transitions. Fig. 3(a) illustrates that $\varepsilon_1(0)$ at the static limit is approximately 14.24, signifying a significantly elevated dielectric constant indicative of substantial polarizability. The positive range of ε_1 indicates wave propagation, but the negative values exceedingly approximately 6.8 eV denote absorption phenomena linked to the plasmon frequency (ω_p). The significant low-energy peak of ε_1 is located within the visible spectrum, highlighting the material's potential applicability in optoelectronic devices. Likewise, $\varepsilon_2(\omega)$ has a peak about 6.22 eV, ascribed to interband electronic transitions from the valence band to the conduction band. At elevated photon energies, ε_2 progressively decreases and disappears around 17.4 eV, indicating a reduced absorption capacity in this range.

The absorption coefficient spectrum, shown in Fig. 3(b), indicates that absorption in the visible and infrared ranges (below 3 eV) is comparatively minimal, affirming broad yet moderate photon harvesting within this range. Notable absorption features appear in the ultraviolet (UV) spectrum above approximately 3.5 eV, peaking around 8–9 eV and exhibiting oscillatory peaks extending to 20 eV. This robust UV absorption suggests possible applications in UV optoelectronics while simultaneously facilitating solar photon capture in the visible range.

The refractive index spectra elucidate light–matter interactions in Sr_3BiI_3, as illustrated in Fig. 3(c). The static refractive index, $n(0)$ ($n(0) = \sqrt{\varepsilon_1(0)}$) is roughly 3.79 for the real component and 0.41 for the imaginary component. As energy increases, $n(\omega)$ initially exhibits a minor reduction before thereafter rising to attain maximum of 2.74 and 1.57 at photon energies of 1.5 eV and 7.04 eV, respectively. These peaks indicate robust photon–electron interaction, signifying spectrum regions with increased optical activity.

The reflectance spectrum of Sr_3BiI_3 underscores its optical flexibility, demonstrated in Fig. 3(d). At zero frequency, the static reflectivity is around 0.34, indicating moderate reflection at low photon energies. As energy increases, reflectivity declines, subsequently displaying a significant peak ($\sim$0.33) about 7.4 eV, then declining to practically zero at approximately 18 eV. This trend indicates that Sr_3BiI_3 exhibits more transparency at elevated photon energies, which is advantageous for PV applications as diminished surface reflection improves light absorption.

The optical conductivity spectrum, depicted in Fig. 3(e), offers additional insight into transport caused by radiative interactions. The real component of conductivity initiates an increase from approximately 1.12 eV to a peak of 4.16 at 6.56 eV, subsequently diminishing towards zero beyond 18 eV, indicating insulating characteristics at elevated photon energy. The imaginary component demonstrates an inverse trend, aligning with the dielectric response of the materials. The energy loss function (L) spectrum, which measures energy dissipation by high-velocity electrons, reveals negligible losses in the infrared and visible areas, therefore facilitating efficient light transmission and absorption across the solar spectrum.[42]

Fig. 3(f) illustrates the energy loss function, where a prominent peak is observed at approximately 15.1 eV, linked to plasma resonance resulting from collective electron oscillations, succeeded by a steep decrease at elevated energies. This verifies that plasmonic effects in Sr_3BiI_3 predominantly manifest in the UV spectrum, much outside the scope of viable solar energy applications. The findings indicate that Sr_3BiI_3 possesses a high dielectric constant, moderate refractive index, robust UV absorption, and low reflectivity, rendering it a viable candidate for advanced optoelectronic and PV applications, where efficient photon capture and minimal energy dissipation are essential for optimal performance.

3.2. Examination of SCAPS-1D results

3.2.1. Design and analysis of solar cell device architecture. The development of efficient and reliable lead-free APSCs necessitates meticulous consideration of device architecture and material choice. This paper proposes and evaluates the architecture of a Sr_3BiI_3-based anti-perovskite device utilizing a n–i–p configuration, optimized for long-wavelength photon absorption and improved charge separation. Fig. 4(a) illustrates the conceptual design of the primary solar cell. The structure consists of several functional layers, with Sr_3BiI_3 acting as the absorber material. This material selection is especially beneficial, as its heterostructure facilitates effective photon absorption and charge retention. The n–i–p configuration enhances sensitivity to long-wavelength radiation relative to traditional semiconductors. Prolonged illumination allows photons to penetrate deeper into the cell, promoting the formation of

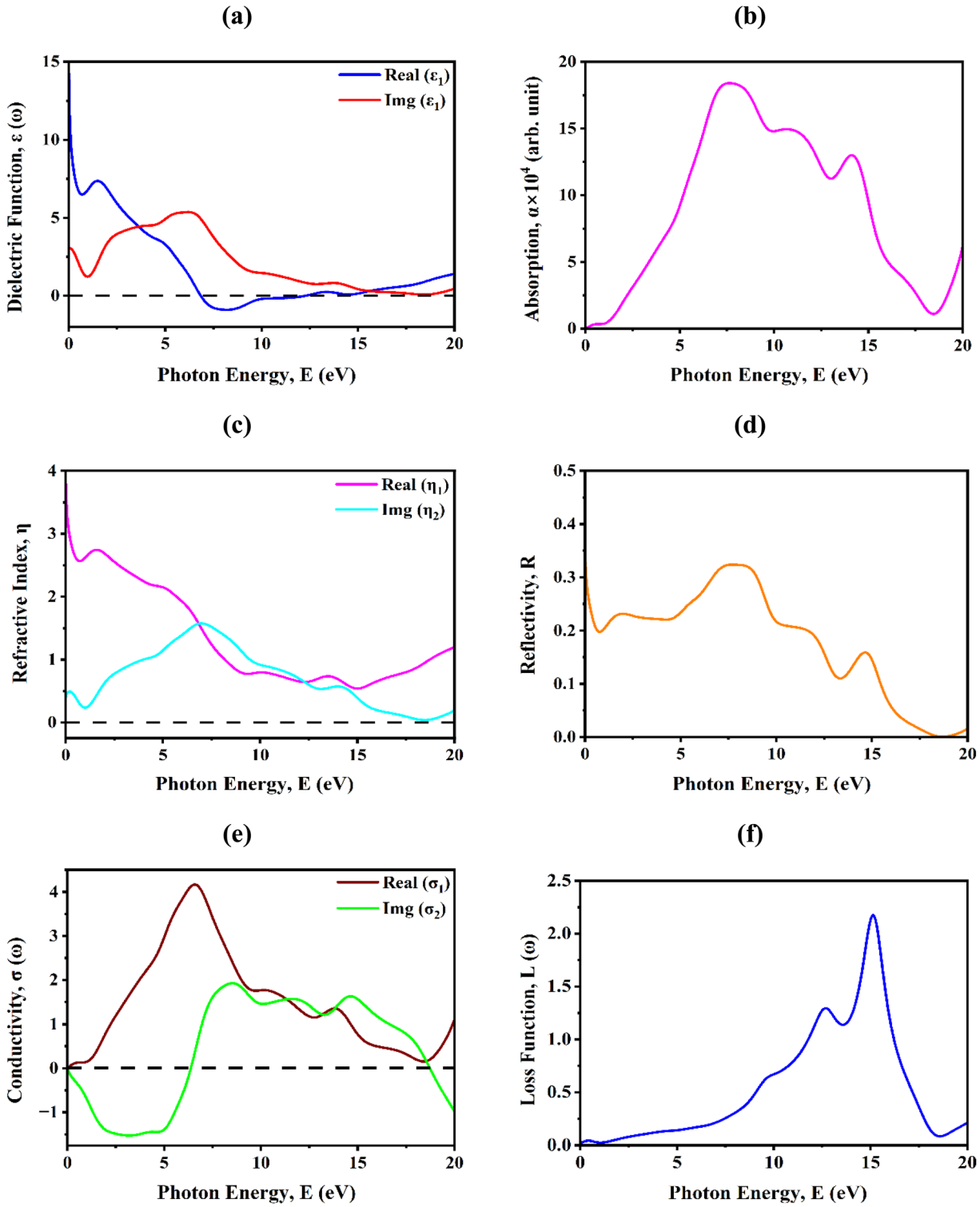

Fig. 3 The optical response of Sr_3BiI_3 anti-perovskite was systematically analyzed through its (a) dielectric function, (b) absorption behavior, (c) refractive index, (d) reflectivity, (e) optical conductivity, and (f) electron energy loss spectrum.

electron–hole pairs (EHPs) both within and outside the depletion region.[42] The expansion of the depletion width immediately improves the creation, separation, and collection of EHPs, hence enhancing the quantum efficiency (QE) of the device. Fig. 4(a) and (b) illustrates the comprehensive device architecture and the energy band alignment of the Al/FTO/ETL/Sr_3BiI_3/HTL/Ni structure, with CBTS, CFTS, CuI, CuSCN, $MASnBr_3$, Sb_2S_3, and SnSe functioning as HTL, Ni and Al serving as the rear and front metallic contacts, and WS_2, IGZO, PCBM, and SnS_2 identified as potential ETLs. Tables 1 and 2

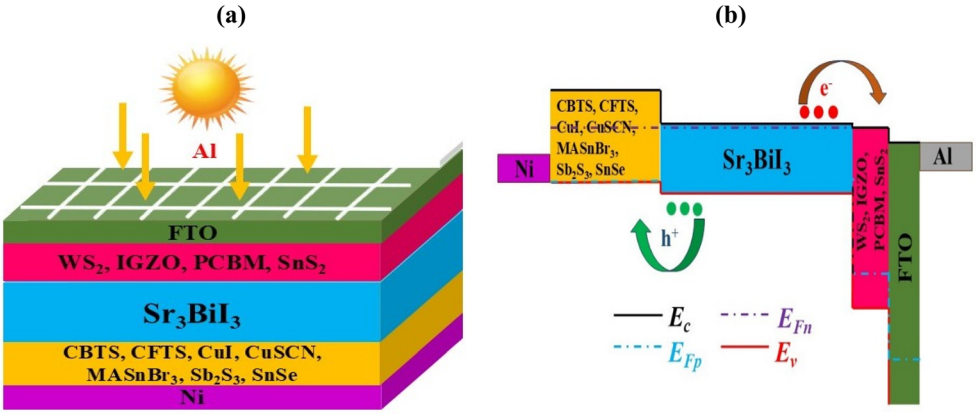

Fig. 4 Examining the (a) crystal structure and (b) energy band alignment of Sr_3BiI_3 with various ETL materials.

encapsulate the simulated input values, whereas Table 3 delineates the parameters employed to model interface defect layers. The SCAPS-1D simulator was utilized to assess device performance, facilitating a systematic analysis of anti-perovskite solar cell architectures under standard operating conditions.

3.2.2. HTL and ETL selection. This study assesses the effectiveness of SCs utilizing four ETLs (WS_2, IGZO, PCBM, and SnS_2) in conjunction with different HTLs, as depicted in Fig. 5(a)–(d). It emphasizes the impact of each ETL on critical PV metrics, including V_{OC}, J_{SC}, FF and PCE across various HTLs in Sr_3BiI_3-based SCs. Out of 28 unique combinations, we identified the four most efficient architectures for comprehensive examination. Fig. 5(a) clearly illustrates the variance of V_{OC} through the assessed ETL-HTL combinations. Among the ETLs, PCBM attained the peak V_{OC} of 0.874 V, whereas IGZO demonstrated the lowest V_{OC} at 0.591 V. Fig. 5(b) illustrates that the J_{SC} values for all devices, excluding the CuSCN HTL, varied from 37.352 to 40.203 mA cm^{-2}, with the combination of CuSCN and IGZO ETL yielding the lowest J_{SC} of 34.804 mA cm^{-2}. Concerning the FF, IGZO demonstrated the lowest value at 59.33%, whereas SnS_2 displayed the highest FF at 86.32%, as illustrated in Fig. 5(c). Significantly, SnS_2 ETL exhibited a superior performance compared to all other ETLs. Fig. 5(d) illustrates a performance comparison of the FTO/ETL/Sr_3BiI_3/HTL/Ni device design, indicating that ETLs like WS_2, IGZO, and SnS_2 consistently attained power conversion efficiencies exceeding 30%, while the PCBM-based ETL achieved a reduced efficiency of 29.18%. This investigation analyzed seven unique HTLs, identifying the most excellent combinations with four unique ETL configurations.

When combined with the CBTS HTL, all ETLs exhibited strong performance, with PCEs varying from 29.18% to 30.31%. CBTS is distinguished as a potential hole transport layer for APSCs due to its optimal bandgap, elevated absorption coefficient, superior conductivity, and advantageous valence band alignment, all of which promote its efficiency in hole transport and hence improve PV performance.

3.2.3. Band adjustment and lattice mismatch of Sr_3BiI_3 absorber with a variety of ETLs. Fig. 6(a)–(d) displays the band alignment of different heterostructures utilizing the Sr_3BiI_3 absorber. This picture depicts the maxima of the valence band (E_V), the minima of the conduction band (E_C), and the quasi-Fermi levels for electrons and holes (F_n and F_p). F_n and E_C sustain a harmonious relationship, but F_p corresponds with E_V throughout various sorts of ETLs. When CBTS serves as HTL, F_n and E_V maintain a consistent energy level throughout all ETLs, resulting in F_n intersecting with E_C, so impeding the transport of both holes and electrons between the ETLs and the HTL. A rear contact (Ni), possessing a 5.5 eV work function (WF), efficiently captures holes from the HTL, whereas front electrode (Al), possessing a work function of 4.1 eV, adeptly collects electrons.

Table 1 Absorber, ETL, and FTO layer modeling and simulation parameters for PV devices.[8,43–45]

Parameters	FTO	Sr_3BiI_3	WS_2	IGZO	PCBM	SnS_2
T (nm)	100	1000	50	50	50	50
E_g (eV)	3.60	1.164	1.8	3.05	2	2.24
ε (eV)	9.0	14.24	13.6	10	9	10
χ (eV)	4.0	4.22	3.9	4.16	3.9	4.24
N_v (cm^{-3})	1.8×10^{19}	2.09×10^{19}	1.8×10^{19}	5×10^{18}	2.5×10^{19}	1.8×10^{19}
N_c (cm^{-3})	2.2×10^{18}	8.43×10^{18}	2.2×10^{18}	5×10^{18}	2.5×10^{19}	2.2×10^{18}
μ_n ($cm^2\ V^{-1}\ s^{-1}$)	100	80	100	15	0.2	50
μ_h ($cm^2\ V^{-1}\ s^{-1}$)	25	25	100	0.1	0.2	50
N_D (cm^{-3})	1×10^{19}	0	1×10^{18}	1×10^{19}	1×10^{18}	1×10^{19}
N_A (cm^{-3})	0	1×10^{18}	0	0	0	0
N_t (cm^{-3})	1×10^{15}	1×10^{14}	1×10^{15}	1×10^{15}	1×10^{15}	1×10^{15}

Table 2 Input parameters for different HTLs.[46–48]

Parameters	CBTS	CFTS	CuI	CuSCN	$MASnBr_3$	Sb_2S_3	SnSe
T (nm)	100	100	100	100	100	100	100
E_g (eV)	1.9	1.87	3.1	2.96	2.15	1.7	1.2
ε (eV)	5.4	9	6.5	10	8.2	7.08	10
χ (eV)	3.6	3.3	2.1	1.7	3.39	3.7	4.2
N_v (cm^{-3})	1.8×10^{19}	2.8×10^{19}	1×10^{19}	1.8×10^{18}	1×10^{18}	1×10^{19}	4.75×10^{18}
N_c (cm^{-3})	2.2×10^{18}	2.2×10^{18}	2.8×10^{19}	2.2×10^{19}	1×10^{18}	2×10^{19}	2.8×10^{18}
μ_n ($cm^2\ V^{-1}\ s^{-1}$)	30	21.98	100	100	1.6	9.8	150
μ_h ($cm^2\ V^{-1}\ s^{-1}$)	10	21.98	43.9	25	1.6	10	100
N_D (cm^{-3})	0	0	0	0	0	0	0
N_A (cm^{-3})	1×10^{19}	1×10^{20}	1×10^{20}	1×10^{20}	1×10^{18}	1×10^{18}	1×10^{18}
N_t (cm^{-3})	1×10^{15}	1×10^{15}	1×10^{15}	1×10^{15}	1×10^{15}	1×10^{15}	1×10^{15}

A crucial determinant of device efficiency is the lattice compatibility between the absorber and transport layers. The lattice mismatch (δ) is determined using eqn (1).[49]

$$\delta = \frac{2|a_s - a_e|}{(a_s + a_e)} \quad (1)$$

where, a_s and a_e signify the lattice constants of the substrate and epitaxial thin film, respectively, and δ indicates the extent of lattice mismatch.

Table 4 delineates the lattice constants and mismatch percentages of Sr_3BiI_3 in relation to several ETL materials. Significantly, Sr_3BiI_3 demonstrates the minimal lattice mismatch with SnS_2 at 24.5%, whereas alternative ETLs present considerably greater mismatches. These findings underscore the significance of lattice engineering in the design of heterojunction-based anti-perovskite devices. Table 5 consolidates the performance outcomes for the Al/FTO/ETL/Sr_3BiI_3/CBTS/Ni structure for four distinct ETL setups. These simulations elucidate the structural compatibility and electrical interactions at the absorber–ETL interface, paving the door for enhanced optimization of lead-free anti-perovskite solar cell topologies.

3.2.4. Assessing the joint impact of defect density (N_t) and absorber layer thickness on PV performance. The thickness of the anti-perovskite absorber layer significantly influences solar cell efficiency. A thin layer leads to inadequate light absorption, whereas a thick layer obstructs charge carrier mobility, impeding efficient transfer to the electrodes.[50] Optimal thickness is essential for enhancing solar cell performance. Thicker absorber layers are associated with a higher number of defects, which can diminish carrier diffusion length and elevate recombination rates. This ultimately leads to reduced overall performance by shortening the lifespan of charge carriers and facilitating recombination prior to their arrival at the electrodes.

This work systematically changed the active layer thickness from 0.2 to 2.0 μm, maintaining the N_t between 10^{10} and 10^{18} cm^{-3}.

Fig. 7(a)–(d) illustrate substantial reductions in V_{OC} as N_t increases, with V_{OC} diminishing from 0.9409 to 0.5460 V for WS_2, from 0.9275 to 0.5427 V for IGZO, from 1.0389 to 0.6702 V for PCBM, and from 0.9860 to 0.5433 V for SnS_2. The relationship between V_{OC} and Sr_3BiI_3 layer depth suggests that while wider layers typically harbor more flaws that hinder performance, thinner layers frequently demonstrate enhanced efficiency due to less recombination.[51] According to the findings, when the absorber depth falls between 0.6 and 1.2 μm, and N_t stays below 10^{14} cm^{-3}, V_{OC} undergoes only a minor decrease, suggesting that the carrier diffusion length and lifetime remain comparatively steady under these circumstances. Among the ETLs, the PCBM structure demonstrated the greatest V_{OC}, whilst the IGZO structure revealed the lowest V_{OC}, highlighting the essential influence of material selection and absorber layer characteristics on SC performance.

Concerning J_{SC}, Fig. 8(a)–(d) illustrate that augmenting the Sr_3BiI_3 layer thickness beyond 0.8 μm, while keeping N_t below 10^{14} cm^{-3}, markedly improves J_{SC}. This enhancement is ascribed to the augmented surface space of the active layer, which optimizes light absorption and produces a higher quantity of charge carriers.[52] Nonetheless, if N_t over a specific threshold, J_{SC} commences to diminish owing to increased recombination losses. The optimized PSC structures with all ETLs attained approximately 40.19 mA cm^{-2} for J_{SC}, signifying highly efficient charge collection under ideal conditions.

Fig. 9(a)–(d) illustrates that the FF diminishes with an increase in both N_t and absorber layer depth. Particularly, FF decreased from 87.25% to 64.16% for WS_2, from 87.27% to 68.76% for IGZO, from 86.32% to 40.27% for PCBM, and from 87.15% to 68.87% for SnS_2 as N_t escalated. The FF maintains relative stability within this range, mirroring the patterns in V_{OC}. In APSCs with inorganic ETLs, intermediate defect densities may improve FF, potentially because specific defects act as passivation sites that alleviate the impact of deeper trap states.

Table 3 Properties of the interface in the suggested heterojunction solar cells

Interface	Defect types	σ_e (cm^2)	σ_h (cm^2)	E_r	Energetic distribution	Density of defect (cm^{-2})
HTL/Sr_3BiBr_3 Sr_3BiBr_3/ETL	Neutral	10^{-19}	10^{-19}	0.6	Single	10^{10} to 10^{17}

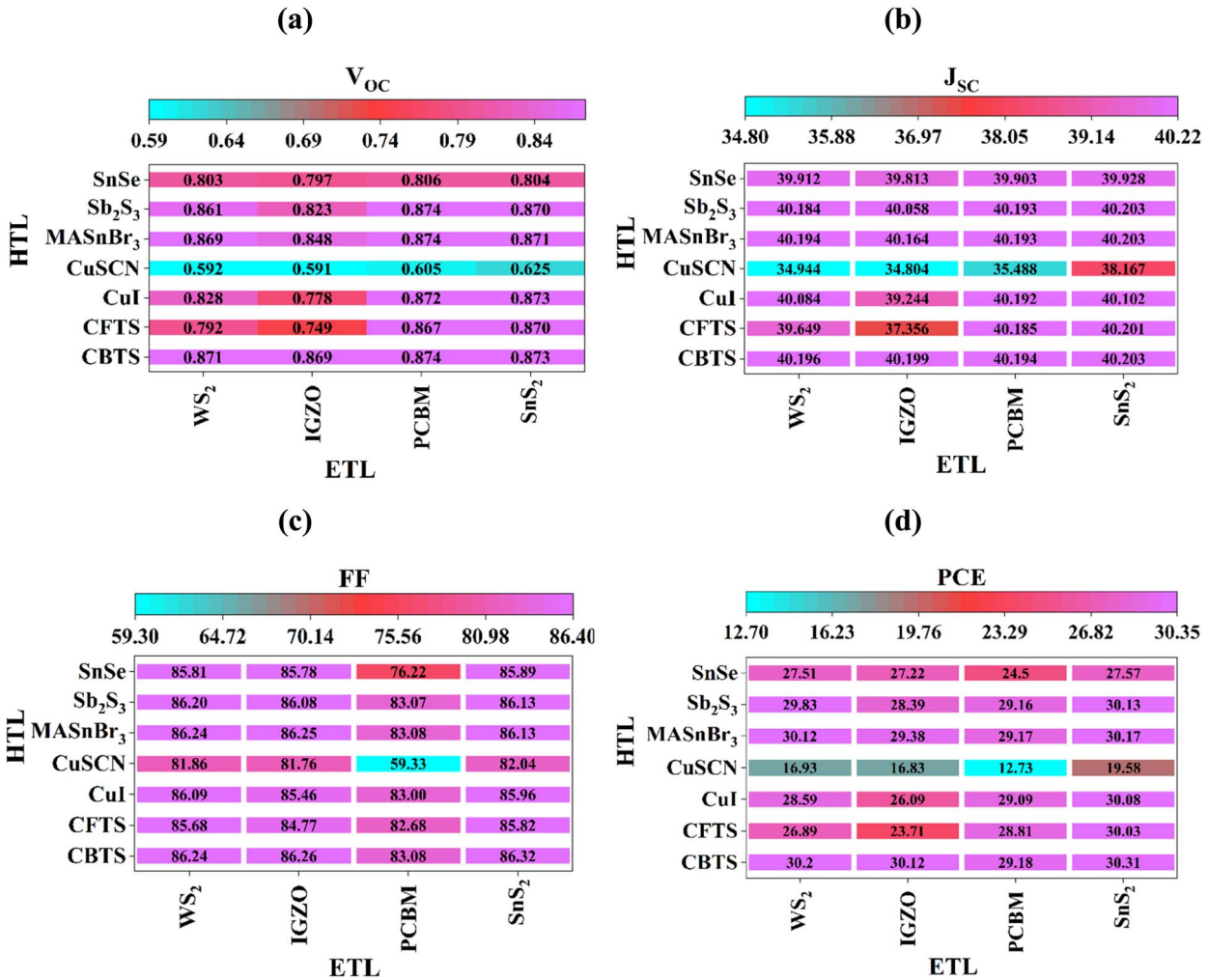

Fig. 5 Investigation of the variations in (a) V_{OC}, (b) J_{SC}, (c) FF, and (d) PCE in Sr_3BiI_3 solar cells with different transport layers.

Fig. 10(a)–(d) demonstrates a notable decline in PCE as the thickness and N_t of the Sr_3BiI_3 layer increases.

The PCE for structures utilizing WS_2, IGZO, PCBM, and SnS_2 ETLs diminished from 33.59% to 8.70%, 33.12% to 9.13%, 36.48% to 2.38%, and 35.12% to 9.26%, respectively. The PCBM-based structure had the most significant decline in PCE, showing heightened sensitivity to increased N_t and layer thickness. The results indicate that PCE is more advantageous when the absorber layer depth exceeds 1 μm, if N_t remains under 10^{14} cm^{-3}. The results highlight the synergistic impact of photoactive layer thickness and N_t on PSC performance, pinpointing an ideal thickness of around 1 μm and N_t near 10^{14} cm^{-3} as the most advantageous combination for enhancing light absorption and carrier transport efficiency.

3.3. Enhancing SC efficiency by the optimization of carrier concentration (N_A) in the absorber layer

To examine the impact of N_A on the absorber's PV properties, the Sr_3BiI_3 layer's N_A was altered between 10^{10} to 10^{19} cm^{-3}. Fig. 11 illustrates the variation of PV characteristics in relation to differing N_A levels. As N_A rose, the V_{OC} stayed largely stable at a nearly constant amount. The hole's Fermi energy level decreases when the absorber layer's N_A rises, thereby leading to an increase in V_{OC}, in accordance with previous findings.[53]

The increase in N_A also leads to a rise in the built-in potential, further augmenting the enhancement of V_{OC}. The enhancement in charge separation is another aspect contributing to the rise in V_{OC}. In all four device configurations, the J_{SC} demonstrated negligible fluctuation as the N_A climbed to 10^{18} cm^{-3}. Nonetheless, except for the SnS_2 ETL, the performance of J_{SC} in the remaining three devices commenced a drop once N_A above this level. However, when the Sr_3BiI_3 layer's N_A went above 10^{15} cm^{-3}, the PCE improved. The devices exhibited maximum V_{OC} values of 0.9157 V, 0.8699 V, 0.9575 V, and 0.8898 V; J_{SC} values of 40.196 mA cm^{-2}, 40.199 mA cm^{-2}, 40.193 mA cm^{-2}, and 40.203 mA cm^2; FF of 86.246%, 86.294%, 85.099%, and 86.34%; and peak PCE values of 30.22%, 30.17%, 29.25%, and 30.37% for the four devices. Table 5 provides a comparative overview of the PV characteristics of devices employing WS_2, IGZO, PCBM, and SnS_2 ETLs.

3.3.1. Examination of ETL layer thickness, doping concentration (N_D) and N_t for enhanced SC efficiency. The transmittance of APSCs can be improved, and recombination

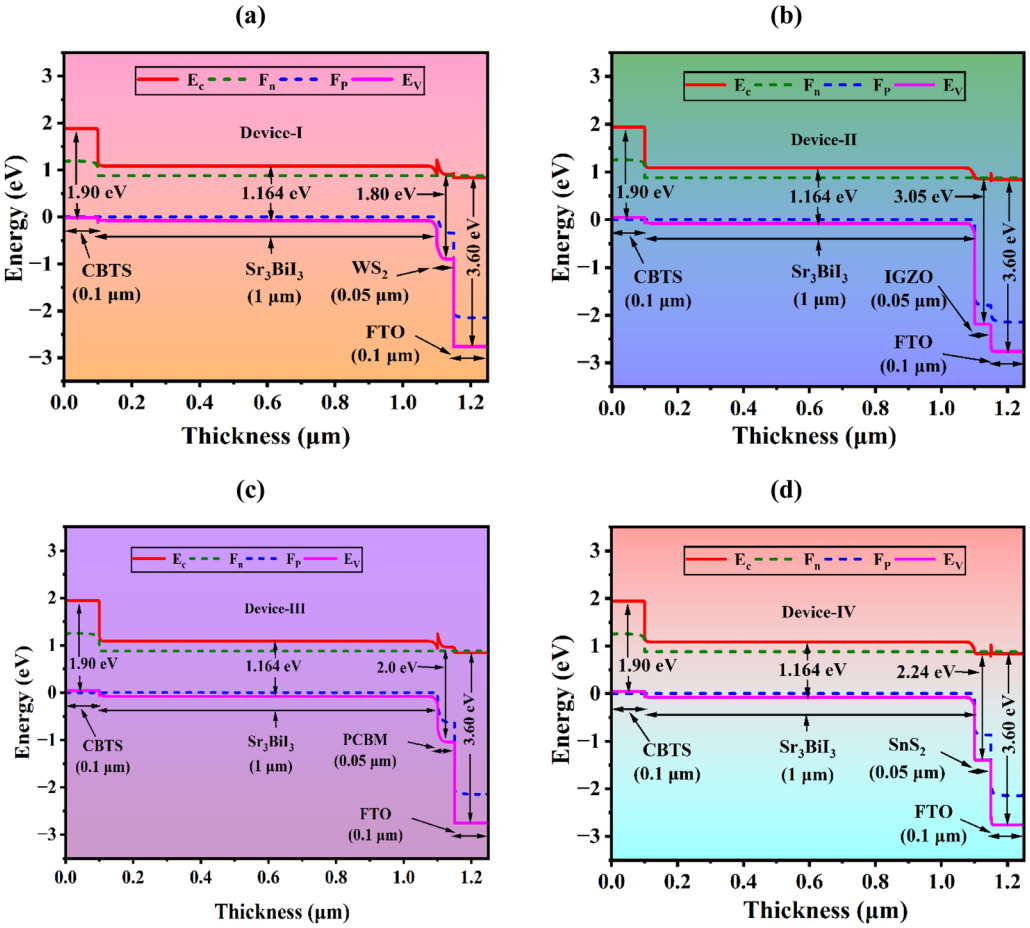

Fig. 6 Modeled band alignment of APSCs employing different ETLs: (a) WS_2, (b) IGZO, (c) PCBM, and (d) SnS_2 with Sr_3BiI_3 as the absorber.

Table 4 Comparison of lattice mismatch for ETL layers with Sr_3BiI_3 absorber

	Lattice parameters			
Layers	*a* (Å)	*b* (Å)	*c* (Å)	Lattice mismatch
Sr_3BiI_3	6.845	6.845	6.845	—
SnS_2	8.76	8.76	9.82	24.5%
WS_2	10.1	10.1	10.4	38.4%
IGZO	3.65	3.65	5.89	60.9%
PCBM	3.15	3.15	12.32	73.9%

Table 5 A comprehensive comparison of PV parameters for various ETL materials in SCs

Device model	V_{OC} (V)	J_{SC} (mA cm^{-2})	FF (%)	PCE (%)
Al/FTO/SnS_2/Sr_3BiI_3/CBTS	0.8733	40.203	86.32	30.31
Al/FTO/WS_2/Sr_3BiI_3/CBTS	0.8711	40.1964	86.24	30.20
Al/FTO/IGZO/Sr_3BiI_3/CBTS	0.8685	40.1992	86.26	30.12
Al/FTO/PCBM/Sr_3BiI_3/CBTS	0.8738	40.1936	83.08	29.18

currents diminished, by selecting a suitable ETL. This study altered the thickness of the WS_2, IGZO, PCBM, and SnS_2 ETLs between 25 nm and 300 nm, keeping other factors constant. Fig. 12(a) illustrates the influence of ETL thickness on PV characteristics. Aside from PCBM, variations in the depth of the ETL exhibited negligible impacts on the V_{OC}, FF, and PCE. The uniformity of the ETL layer thickness throughout a broad spectrum demonstrates the adaptability of the film production technique, which may be modified for implementation in the suggested device topologies.[54] Nonetheless, when the ETL thickness augmented, transmittance diminished, leading to a significant reduction in performance, in accordance with prior studies.[17] The PCE for the PCBM ETL decreased from 29.18 to 26.59%, FF from 83.11 to 82.92%, J_{SC} from 40.20 to 36.78 mA cm^{-2}, and V_{OC} from 0.8735 to 0.8718 V. For the WS_2 and SnS_2 ETLs, J_{SC} and V_{OC} exhibited relative stability, with measurements of 40.18 mA cm^{-2} and 0.8711 V for WS_2, and 40.19 mA cm^{-2} and 0.8727 V for SnS_2, respectively. PCE and FF exhibited minor variations, oscillating between 30.190% and 30.174% and 86.2399% and 86.2159% for WS_2, and between 30.28% and 30.25% and 86.30% and 86.27% for SnS_2, respectively. For IGZO, performance measurements exhibited a minor decline, with V_{OC} dropping from 0.8699 V to 0.8696 V, J_{SC} from 40.20 mA cm^{-2} to 39.75 mA cm^{-2}, FF from 86.29% to 86.24%, and PCE from 30.181% to 29.826%. The ideal ETL thickness for WS_2, IGZO, PCBM, and SnS_2 ETLs was established at 50 nm.

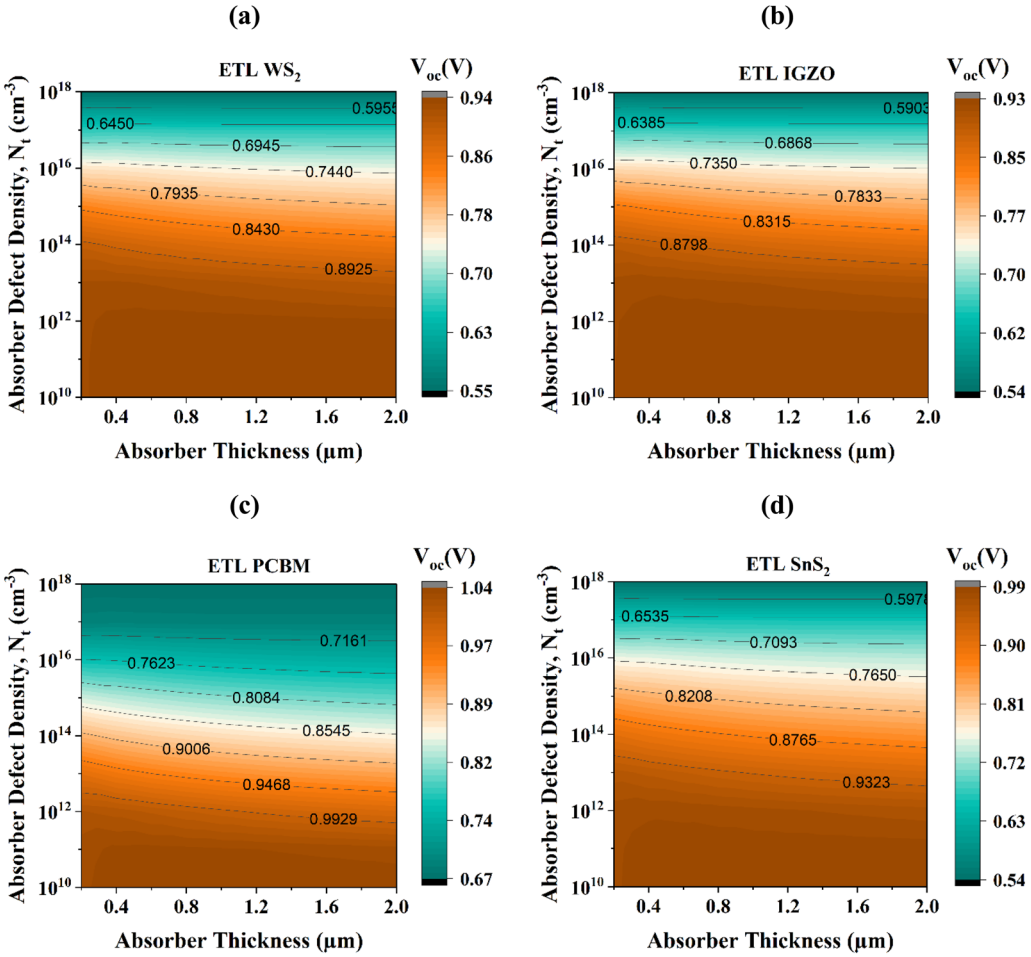

Fig. 7 Examining the impact of N_t and Sr_3BiI_3 thickness on V_{OC} in various ETL configurations: (a) WS_2, (b) IGZO, (c) PCBM, and (d) SnS_2.

Fig. 12(b) illustrates the variation in PV properties as a function of N_D for all ETLs. For IGZO, V_{OC} remained relatively stable at N_D levels below 10^{17} cm^{-3} but declined marginally to 0.7949 V and subsequently climbed to 0.8713 V when N_D went up to 10^{20} cm^{-3} from 10^{18} cm^{-3}. Both J_{SC} and FF had marginal increases, ascending from 40.1775 to 40.19811 mA cm^{-2} and from 86.141 to 86.3305%, respectively, before settling at 10^{18} cm^{-3} for J_{SC} and 10^{19} cm^{-3} for FF. For WS_2 and PCBM, V_{OC} diminished from 0.87416 to 0.87170 V and from 0.9499 to 0.8733 V, respectively, whereas J_{SC} augmented from 39.0637 to 40.1928 mA cm^{-2} and from 13.6356 to 40.1535 mA cm^{-2}. FF progressively rose from 29.2191 to 86.330% and from 19.3737 to 86.3208%, whereas PCE enhanced from 9.9778 to 30.2467% and from 2.5095 to 30.2695% as N_D fluctuates between 10^{12} to 10^{20} cm^{-3}. For SnS_2, performance metrics remained steady until the N_D increased from 10^{10} to 10^{17} cm^{-3}, following which a little decline was succeeded by a marginal increase. The Device-IV utilizing SnS_2 as ETL exhibited optimal performance at $N_D = 10^{19}$ cm^{-3}.

The value of N_t leads to the entrapment of photogenerated carriers, initiating Shockley–Read–Hall (SRH) recombination.[55] An augmentation in carrier concentration diminishes the average free path, consequently enhancing recombination rates. The efficiency of the SCs is markedly diminished by SRH recombination linked to elevated bulk defects. The PV characteristics were predominantly stable up to a N_t of 10^{18} cm^{-3}, except for the PCBM ETL, where minor alterations were noted. To enhance device performance in actual production environments, it is crucial to keep $N_t \leq 10^{15}$ cm^{-3}, as illustrated in Fig. 12(c). Thus, the ideal N_t has been determined to be 10^{15} cm^{-3}, enabling effective material to use and photon transmission in the ETL layer.

3.3.2. Enhancing PV performance by optimizing the N_t at the absorber/ETL interface. The performance of APSCs is significantly influenced by recombination losses at the interfaces between the Sr_3BiI_3 absorber and the ETL. The losses are chiefly attributable to flaws that entrap charge carriers, thereby diminishing their mobility and heightening the probability of recombination.[56] The impact of interface N_t at the Sr_3BiI_3/ETL interface was assessed by varying N_t from 10^{10} cm^{-2} to 10^{17} cm^{-2}, as illustrated in Fig. 13. It is evident from the Fig. that when N_t grows, the performance metrics of the PSC deteriorate due to an elevated recombination rate, leading to a decline in PCE.

The PSC exhibited optimal performance at a N_t value of 10^{14} cm^{-2}, designated as the reference value for further assessment

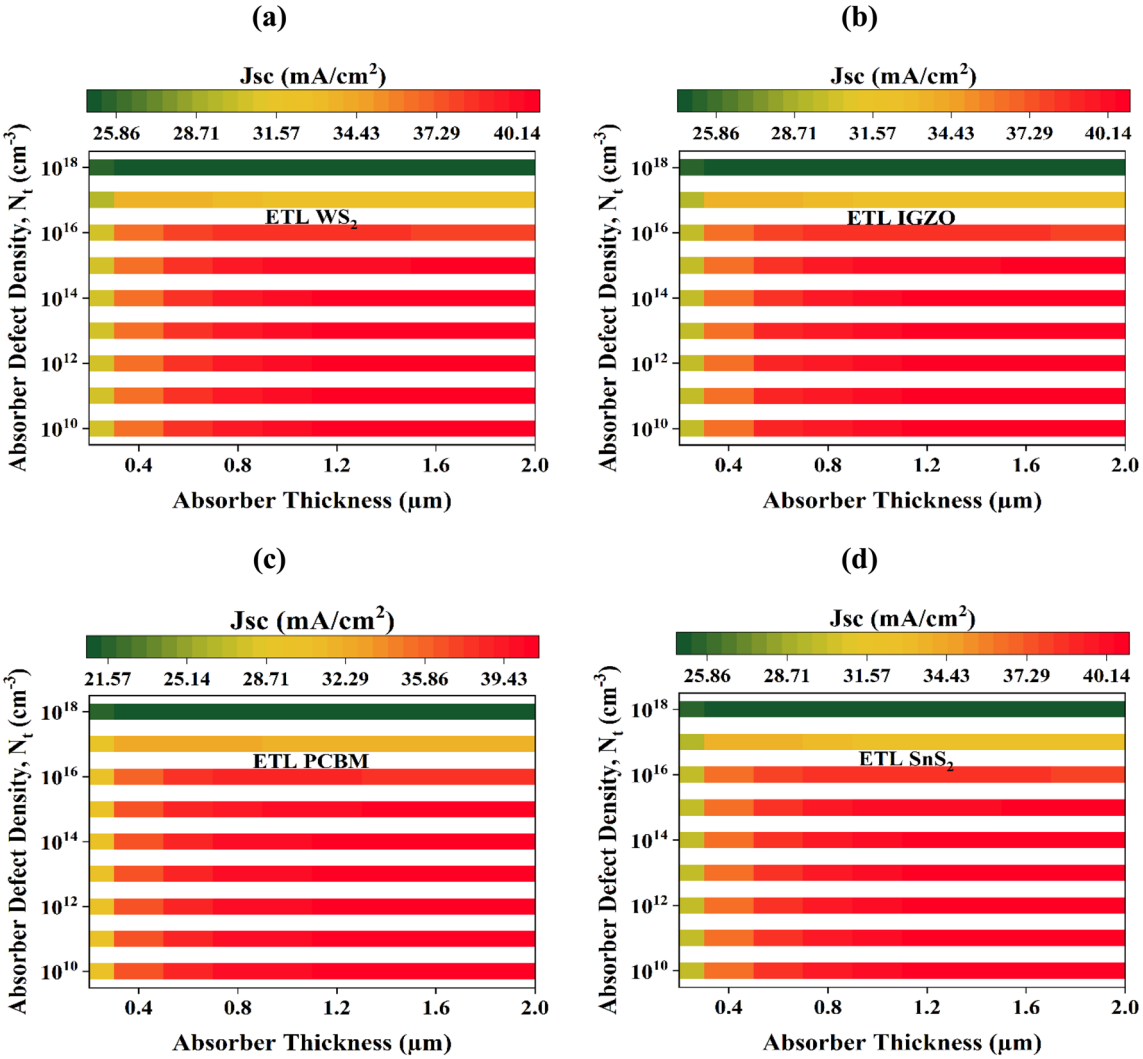

Fig. 8 Examining the impact of N_t and Sr_3BiI_3 thickness on J_{SC} in various ETL configurations: (a) WS_2, (b) IGZO, (c) PCBM, and (d) SnS_2.

in later stages. The selection of the N_t range was determined considering V_{OC}, since it exhibits greater sensitivity to N_t than J_{SC}.[57] Eqn (2) can be utilized to establish the V_{OC} limit resulting from interface recombination:

$$V_{OC} = \frac{1}{q}\left\{\varphi_c - \beta KT \ln\left(\frac{qN_V R_v}{J_{SC}}\right)\right\} \quad (2)$$

where R_v denotes the interface recombination velocity, the ideality factor and effective barrier height are indicated by β and φ_c.

3.3.3. Examining the impact of resistance and temperature on SC performance. Series resistance (R_S) and shunt resistance (R_{Sh}) are essential in influencing the performance of APSCs. Fig. 14(a) demonstrates that R_S originates from contacts, transport layers, and interfaces, with the examined values ranging from 0 to 7 Ω cm^2. It does not influence V_{OC} and has a negligible effect on J_{SC}, which is mostly determined by light absorption and the inherent quality of the material. Nonetheless, R_S markedly diminishes both FF and PCE, with linear reductions of around 30% and 10%, respectively. The FF decline is associated with solder bond degradation, whereas the PCE loss stems from power dissipation and diminished current flow. Therefore, reducing R_S is crucial for optimal performance. Conversely, Fig. 14(b) demonstrates that R_{Sh} arises from leakage channels, including pinholes and recombination losses. The change from 10 to 10^7 Ω cm^2 significantly impacts device performance. As R_{Sh} increases, V_{OC} escalates from 0.4 V to 0.86 V, although J_{SC} remains relatively constant. Increased R_{Sh} diminishes leakage and recombination, enhancing voltage stability and efficiency. At elevated R_{Sh} (>10^4 Ω cm^2), both J_{SC} and V_{OC} reach saturation, constrained by intrinsic material limitations that inhibit additional improvements. Significantly, FF enhances markedly from 25% to 86%, and PCE increases by approximately 25%, underscoring the crucial function of R_{Sh} in mitigating power losses. Enhancing R_{Sh} facilitates improved current conduction, increased peak power output, and performance that approaches theoretical maxima. Minimizing RS and increasing RSH are essential for attaining high-efficiency APSCs. Temperature significantly influences APSCs, as these devices are generally utilized outside and are consistently

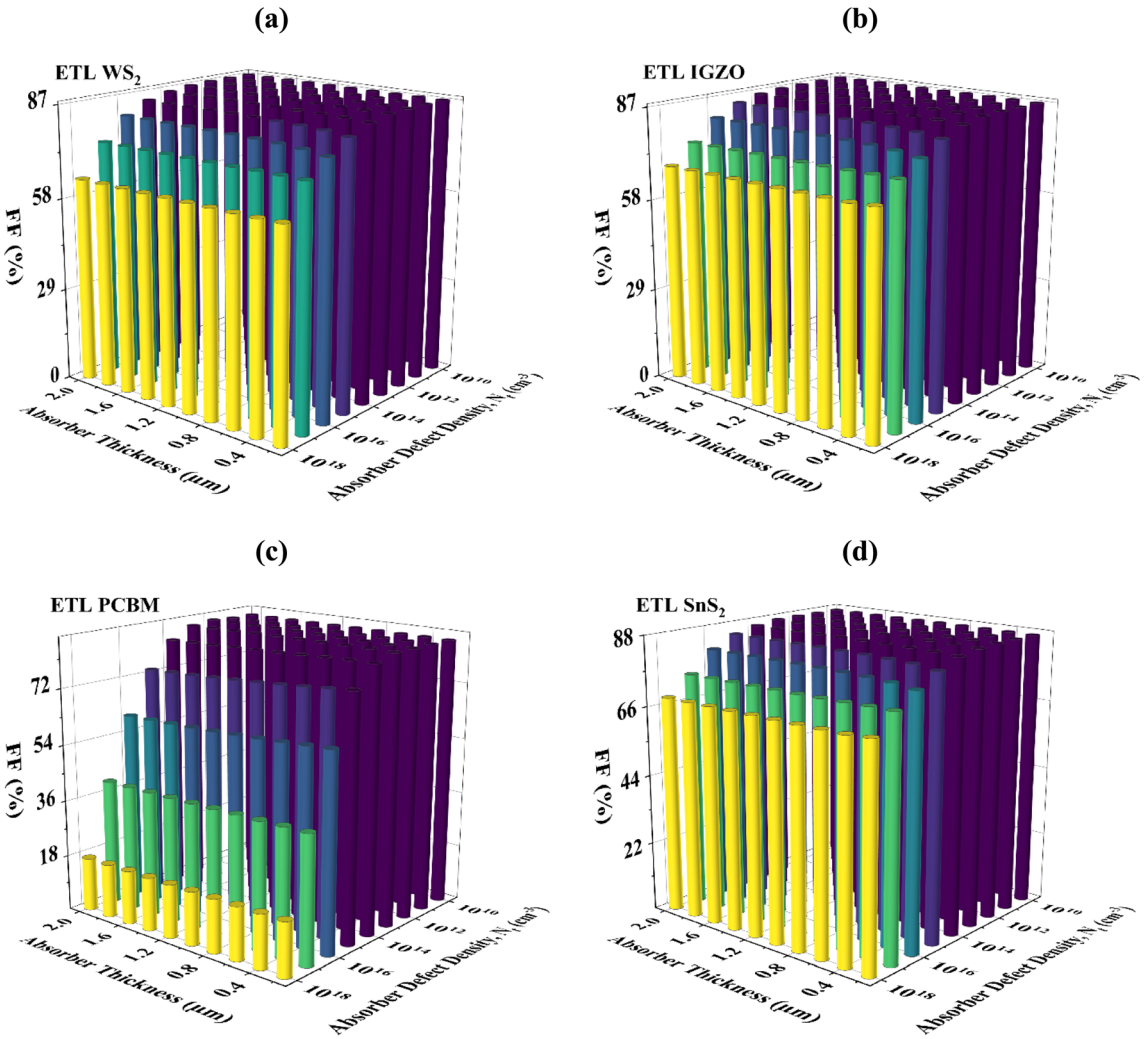

Fig. 9 Examining the impact of N_t and Sr_3BiI_3 thickness on FF in various ETL configurations: (a) WS_2, (b) IGZO, (c) PCBM, and (d) SnS_2.

subjected to AM1.5G sunshine. Consequently, their temperature can rapidly exceed ambient temperature. Recent studies in optoelectronics utilizing anti-perovskites have shown enhancements in device stability and performance under elevated temperatures.[58] Fig. 14(c) shows the temperature varied from 300 K to 475 K to evaluate its effect on the output parameters of APSCs.

The V_{OC} decreases as the temperature rises because higher temperatures cause the reverse saturation current (J_0) to increase, which exhibits an inverse correlation with V_{OC}. Eqn (3) exemplifies this relationship:[59]

$$V_{OC} = \frac{AKT}{q_v}\left[\ln\left(1 + \frac{J_{SC}}{J_O}\right)\right] \quad (3)$$

where the ideality factor is indicated as A, and $\frac{KT}{q_v}$ indicates the thermal voltage. As temperature escalates, fault concentrations inside the material concurrently grow, hence exacerbating the decline in V_{OC}. Moreover, both FF and PCE diminish at elevated temperatures, presumably due to a decline in R_{SH}. It clearly demonstrates that the optimal PCE is achieved at 300 K, equivalent to room temperature. This discovery corroborates earlier research, suggesting that ambient temperature is optimal for PSC efficacy.

3.3.4. *J–V* and QE analysis of SC performance under various conditions. The *J–V* and QE attributes offer critical insights into the PV performance of the Al/FTO/ETL/Sr_3BiI_3/CBTS/Ni combination, wherein WS_2, IGZO, PCBM, and SnS_2 serve as ETLs. Fig. 15(a) demonstrates how the choice of ETL affects the device's overall efficiency. Among the evaluated ETLs, SnS_2 exhibited significantly higher current density values. The current density for WS_2 was around 40.1964 mA cm^{-2}, for PCBM it was 40.1936 mA cm^{-2}, and the peak current density of 40.203 mA cm^{-2} was attained with SnS_2. This indicates that SnS_2 improves the efficiency of charge carrier transport from the absorber layer to the electrodes, a vital element in maximizing the overall performance of APSCs. The photocurrent produced by the device is frequently evaluated by both internal and exterior QE.[60] Internal QE denotes the ratio of EHPs generated to the amounts of photons absorbed in the device's operational layer, serving as a direct indicator of photocurrent generation.[61]

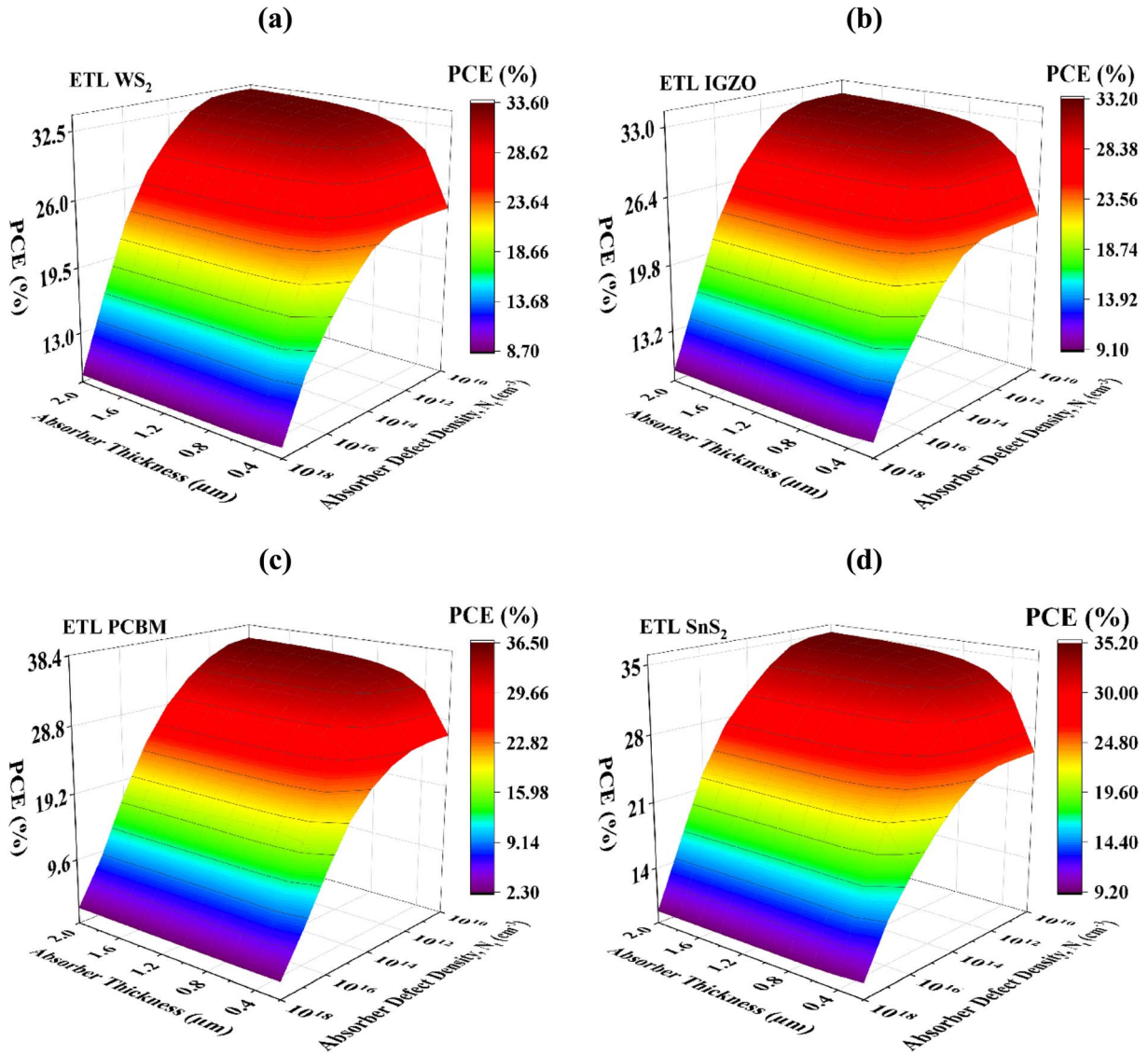

Fig. 10 Examining the impact of N_t and Sr_3BiI_3 thickness on PCE in various ETL configurations: (a) WS_2, (b) IGZO, (c) PCBM, and (d) SnS_2.

Fig. 15(b) displays the QE curves for all four structures, demonstrating the correlation between QE and wavelength. The QE covers a wavelength somewhere between 300 to 1200 nm, beginning at around 100% and gradually diminishing to 0% as the wavelength approaches 1070 nm. The noted decline in QE aligns with the *J–V* characteristic findings, further corroborating the impact of ETL selection on the PV efficacy of the devices.

3.3.5. Nyquist plot. Impedance spectroscopy (IS) was conducted to examine the interfacial charge dynamics and recombination characteristics of APSCs utilizing different ETLs. Fig. 16 illustrates the Nyquist plots that depict the frequency-dependent impedance response of the devices, recorded across a frequency spectrum from 1 Hz to 1 MHz. Each semicircular arc denotes the charge recombination properties, with the diameter of the semicircle reflecting the recombination resistance (R_{rec}) of the system. The WS_2-based device demonstrated a significantly bigger semicircle, signifying elevated R_{rec} and decreased recombination rates relative to alternative ETLs. This enhancement is ascribed to the optimized defect density in the anti-perovskite absorber layer, attained by regulated halide composition and improved crystallization. The mitigation of deep-level trap states and better film uniformity reduces non-radiative recombination, facilitating extended carrier lifetimes and enhanced charge transfer efficiency at the ETL/anti-perovskite interface. Comparable enhancements in recombination behavior by defect reduction have been documented by Jeon *et al.*,[62] substantiating the efficacy of compositional and structural optimization for the improvement of charge transport. The increased R_{rec} in the optimized anti-perovskite structure signifies effective defect passivation, diminishing electronic disorder and stabilizing the Fermi level within the absorber.

This passivation improves the intrinsic electric field, effectively reducing interfacial recombination losses. Conversely, the

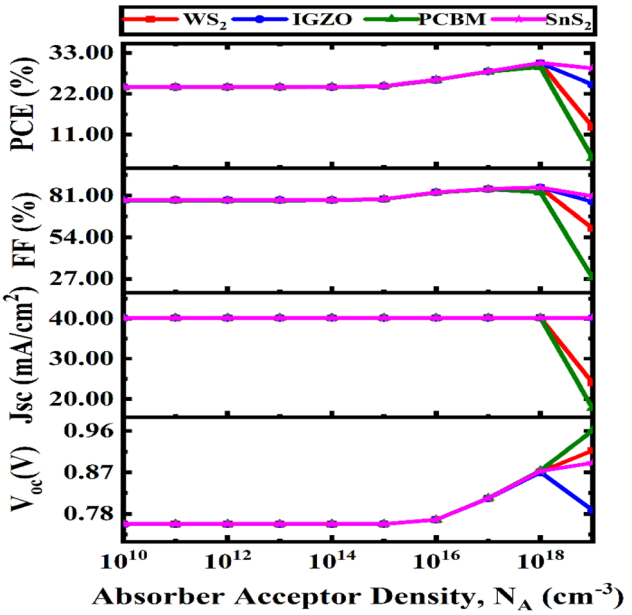

Fig. 11 Analyzing the influence of N_A in Sr_3BiI_3 absorber layer on PV device efficacy.

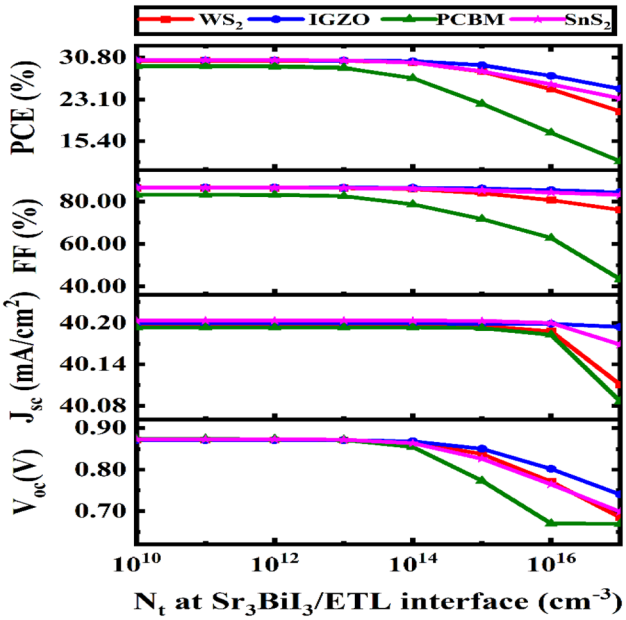

Fig. 13 Fluctuation in Sr_3BiI_3/ETL interface N_t and its effect on SC efficiency.

PCBM-based ETL device exhibited a reduced semicircle, indicating diminished recombination resistance and expedited charge extraction. This phenomenon is ascribed to its advantageous interfacial energy alignment and diminished charge buildup. According to Jiang *et al.*,[63] systems characterized by reduced trap densities and enhanced interface quality consistently demonstrate elevated R_{rec} and clearer Nyquist characteristics, establishing a direct correlation between microstructural optimization and macroscopic performance. At elevated frequencies, capacitance effects indicate charge accumulation at interfacial layers, but at reduced frequencies, the impedance response is affected by ionic migration and hysteresis related to halide ion mobility. Comparable low-frequency inductive characteristics were also observed in previous research.[64,65] The IS analysis verifies that decreasing defect density and refining interface engineering significantly improve recombination resistance, mitigate non-radiative losses, and promote efficient charge transfer. These findings corroborate the material optimization technique and closely correspond with existing literature, highlighting the essential function of defect passivation in enhancing the performance of APSCs.

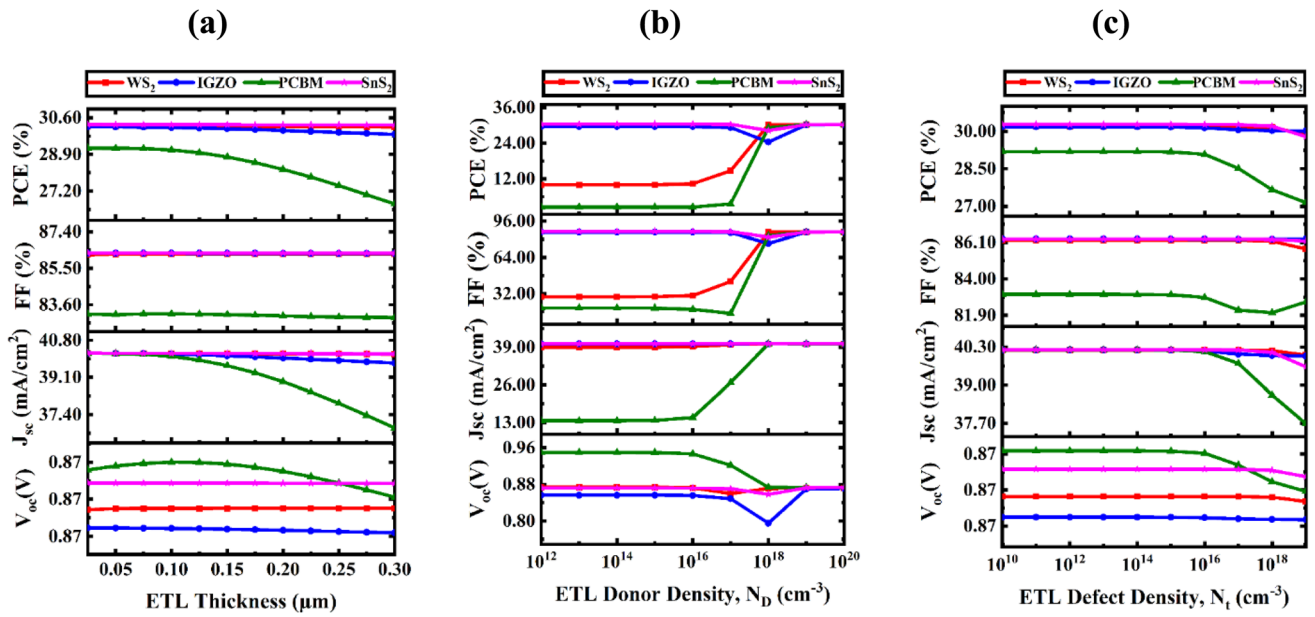

Fig. 12 Thorough examination of (a) thickness, (b) N_D, and (c) N_t in SCs with multiple ETLs.

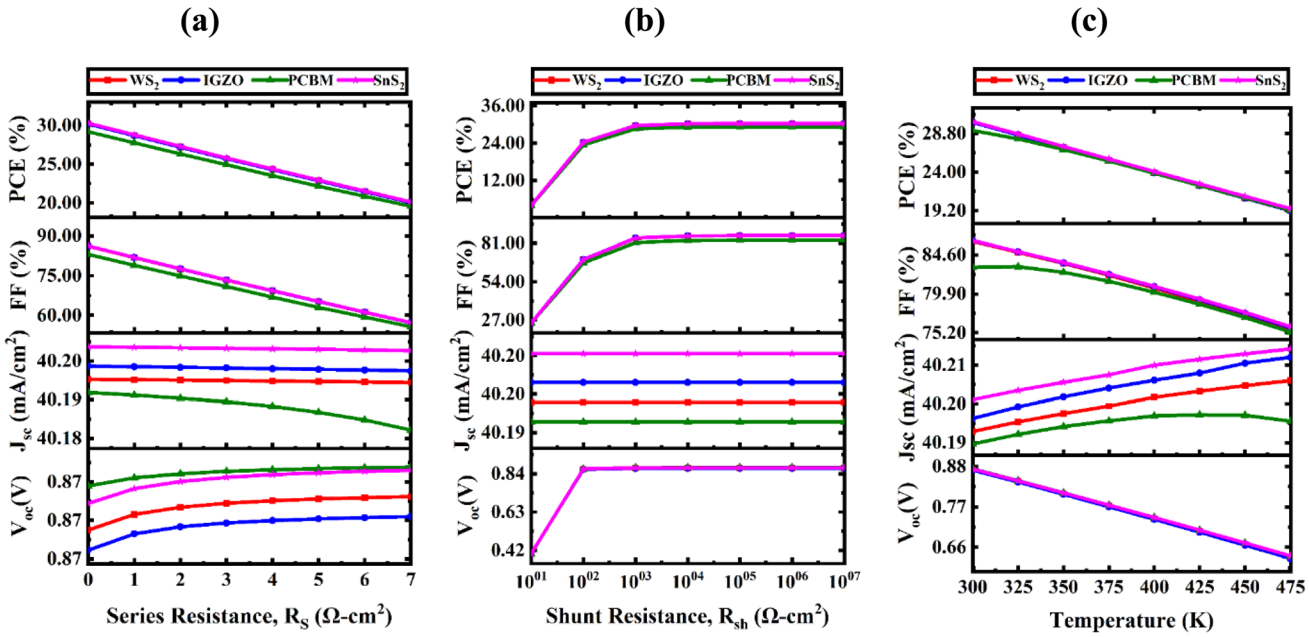

Fig. 14 Impact of (a) series, (b) shunt resistance, and (c) temperature on performance metrics.

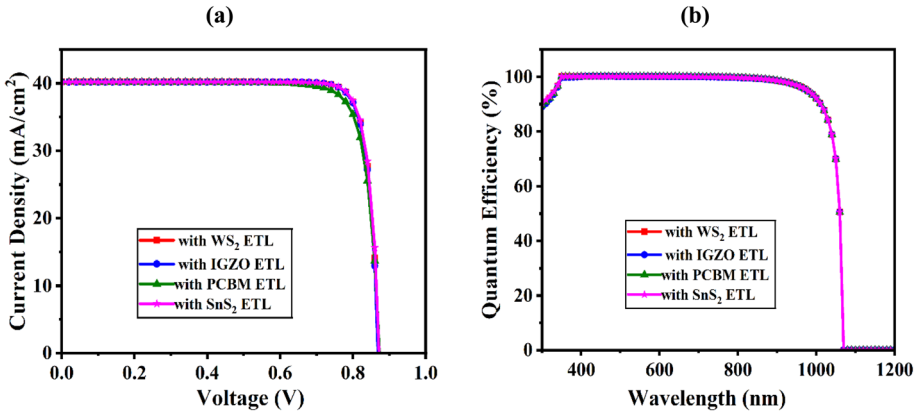

Fig. 15 Comparable (a) *J*–*V* and (b) QE characteristics of all device setups.

3.3.6. Assessment and verification of SCAPS-1D outcomes in light to prior research. This section provides a comparison of optimum SC architectures. The optimum configuration identified through a series of trials was FTO/SnS_2/Sr_3BiI_3/CBTS, with the maximum efficiency of 30.31%. Table 6 presents a comparison of diverse anti-perovskite-based devices published from 2021 to 2025. It indicates that despite the proposal and examination of many device topologies utilizing different ETL and HTL materials, the PCE has always remained below 30% owing to poor J_{SC} values. The diminished J_{SC} values are chiefly ascribed to the extensive bandgap, which constrains the cutoff wavelength and diminishes spectrum usage.[66] The incorporation of SnS_2 markedly enhanced spectrum utilization, resulting in a J_{SC} of 40.203 mA cm^{-2} and a matching PCE of 30.31%, as illustrated in Table 4. This indicates that the integration of SnS_2 as ETL, CBTS as HTL, and Sr_3BiI_3 as photoactive layer produces optimal performance.

This optimized configuration surpasses alternative SC architectures in efficiency. The light-absorbing layer is essential in influencing the overall efficiency of the SC. This study emphasizes that, through systematic experimentation in choosing the suitable ETL, HTL, and their optoelectronic characteristics, the SC architecture is rendered more effective and efficient than other APSCs, despite concurrent investigations by other researchers into the Sr_3BiI_3 light-absorbing layer.

4. Machine learning (ML) integration

Machine learning (ML) serves as an effective instrument in the optimization of material properties and device performance within the domain of APSCs. The capacity to analyze extensive and intricate datasets facilitates the identification of critical factors influencing solar cell efficiency, yielding significant insights for device optimization without necessitating

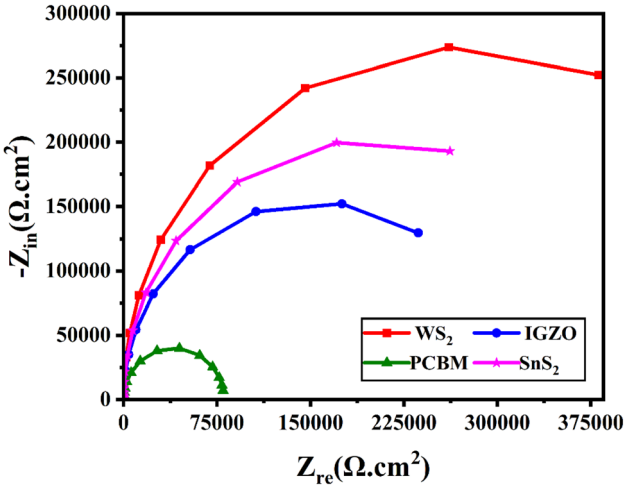

Fig. 16 Impedance characteristics of Sr_3BiI_3-based APSCs utilizing diverse ETL materials: a Nyquist plot examination.

exhaustive experimental trials. This study utilized the Random Forest (RF) algorithm, a powerful machine learning method adept at managing high-dimensional datasets and effectively addressing non-linear relationships among input variables.[75,76] Random Forest is advantageous in this context due to its resilience to overfitting, capacity to model complex interactions, and ability to manage large datasets with multiple features, making it an ideal choice for predicting the performance of APSCs. Alternative machine learning algorithms, including linear regression and support vector regression, were evaluated but deemed to add unnecessary complexity, potentially resulting in overfitting and diminished model performance.[77] Linear regression may inadequately represent complex non-linear relationships among features, whereas support vector regression, in high-dimensional contexts, frequently experiences overfitting, which diminishes the model's predictive accuracy. This corresponds with the principle of "Kolmogorov Complexity," indicating that an increase in data complexity does not guarantee enhanced model accuracy unless the model's complexity is suitably modified.[78] Prior research indicates that dataset simplification or complexity reduction can improve model accuracy and generalizability, which justifies the selection of Random Forest for its balanced complexity-performance approach.[79,80] This study utilized a dataset generated by the SCAPS-1D simulator, comprising ten input features and four target variables. A total of 13 986 samples were utilized for the training and testing of the machine learning model. The extensive and varied dataset facilitated the model's ability to encompass a broad spectrum of data variations, thereby enabling the identification of significant relationships between material properties and device performance.

Fig. 17 presents the Pearson correlation coefficient map, which depicts the relationships among the ten input variables and the four target variables: V_{OC}, J_{SC}, FF, and PCE. This map illustrates the strength of correlations, offering insight into the impact of each feature on solar cell performance.

A significant positive correlation exists between V_{OC} and the absorber's bandgap ($r = 0.69$), whereas negative correlations are noted with interface defect ($r = -0.23$) and bulk defect density ($r = -0.14$), highlighting the critical role of band structure and energy-level alignment. The parameters of thickness, dielectric permittivity, electron mobility, hole mobility, and temperature exhibit weak or negligible correlations, indicating their indirect or coupled effects on performance. J_{SC} demonstrates a significant negative correlation with band gap ($r = -0.97$), highlighting the trade-off between photon absorption and short-circuit current. FF exhibits a positive correlation with band gap ($r = 0.44$) and electron affinity ($r = 0.30$), indicating the influence of energy-level alignment and diminished recombination. PCE exhibits negative correlations with defect density ($r = -0.22$) and interface defects ($r = -0.28$), highlighting the adverse impact of recombination on efficiency. This underscores the importance of optimizing defects, band gap, and energy-level alignment to improve PSC performance.

A Random Forest with 100 decision trees was utilized to capture intricate non-linear interactions and mitigate

Table 6 Comparative analysis of PV parameters of PSC with previous work (E = experimental, T = theoretical)

Types	Device architecture	J_{SC} (mA cm^{-2})	V_{OC} (V)	FF (%)	PCE (%)	Ref.
E	TiO_2/$CsPbBr_3$/Spiro-OMETAD	6.820	1.307	68	6.08	67
E	ITO/CdS/Sb_2Se_3/Au	25.50	0.43	59.30	6.50	68
E	$CsPbI_3$/$FAPbI_3$	17.26	1.22	74	15.60	69
T	Al/FTO/SnS_2/Ba_3NCl_3/Au	38.26	0.94	79.91	28.81	20
T	Ag/FTO/CdS/(Ca_3AsI_3/Ca_3PI_3)/V_2O_5/Ni	25.61	1.33	85.33	29.16	46
T	FTO/SnS_2/Ca_3NCl_3/MoO_3	22.89	1.36	90.36	28.13	47
T	FTO/SnS_2/Ba_3SbI_3	27.51	0.91	85.16	21.29	70
T	ITO/SnS_2/Ba_3PF_3	26.74	0.97	89.25	23.15	71
T	Al/FTO/WS_2/Sr_3PCl_3/Au	20.02	1.063	83.03	17.70	72
T	ITO/LBSO/Cs_2TiBr_6/CNTS/Au	26.63	1.123	82.94	24.82	73
T	FTO/n-TiO_2/p-$CsSnI_3$/p-P3HT	34.70	0.972	78.21	26.40	74
T	FTO/ZnO/Sr_3NCl_3/$MASnBr_3$	19.777	1.56	88.84	27.34	48
T	Al/FTO/SnS_2/Sr_3BiI_3/CBTS/Ni	0.8733	40.203	86.32	30.31	This work
T	Al/FTO/WS_2/Sr_3BiI_3/CBTS	0.8711	40.1964	86.24	30.20	This work
T	Al/FTO/IGZO/Sr_3BiI_3/CBTS	0.8685	40.1992	86.26	30.12	This work
T	Al/FTO/PCBM/Sr_3BiI_3/CBTS	0.8738	40.1936	83.08	29.18	This work

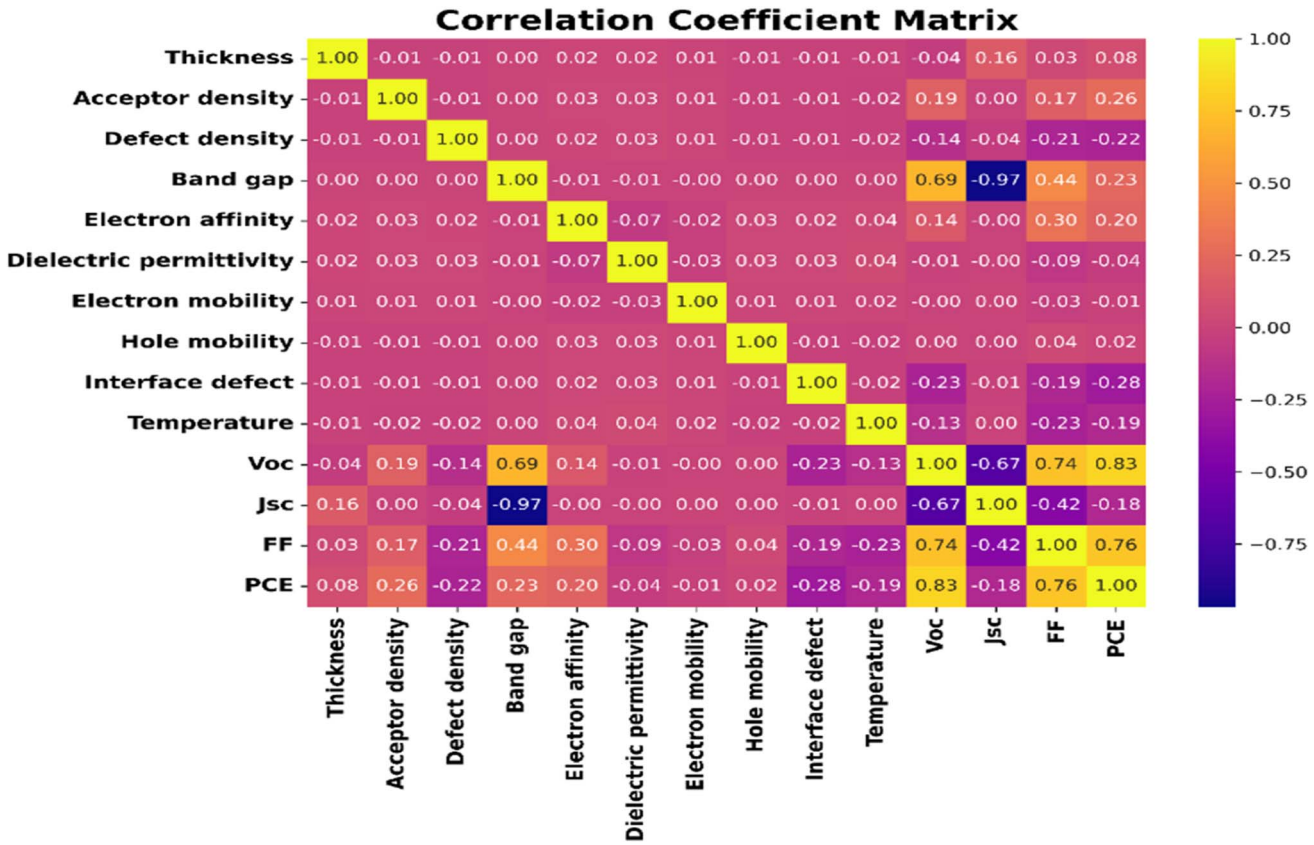

Fig. 17 Pearson correlation coefficient map.

overfitting.[81] Post-training, the predictions of PV parameters compared with actual data, and scatter plots, as depicted in Fig. 18, demonstrated a robust correlation between predicted and actual values, hence affirming the model's reliability.

The model's predictive capabilities were assessed using multiple evaluation measures, including MAE, MSE, RMSE, and MAPE, as illustrated in Fig. 19. RMSE quantifies the difference between expected and actual values, whereas MSE calculates the mean of the squared differences, attributing greater significance to larger errors and rendering it sensitive to outliers.[82,83] Conversely, MAE calculates the average absolute deviation without squaring the errors, resulting in reduced sensitivity to outliers. Additionally, the R^2 is a significant metric that quantifies the proportion of variance in the dependent variable handled by the independent variables.[84] Increased R^2 values indicate enhanced model fit.

The estimated R^2 values for each target variable were V_{OC} = 0.986, J_{SC} = 0.978, FF = 0.973, and PCE = 0.989. The results demonstrate a robust correlation between projected and actual outputs, affirming the model's efficacy in capturing performance trends.

4.1. Feature significant analysis

4.1.1. Relative importance of each feature. The feature importance analysis, performed with Scikit-learn, elucidates the relative significance of several parameters in ascertaining the PCE of Sr_3BiI_3-based APSCs. Fig. 20(a) and (b) illustrates that the three most significant properties are thickness, defect density, and band gap, which collectively have a considerable effect on solar cell performance. Defect density is the paramount factor, since elevated defect densities result in greater recombination losses, hence substantially diminishing efficiency. This corresponds with the recognized notion that imperfections in anti-perovskite materials function as recombination hotspots, obstructing charge carrier passage and collection. The band gap is a crucial parameter, since it determines the material's absorption spectrum and its compatibility with the energy levels of ETLs and HTLs. A band gap that strays from the ideal range leads to diminished light absorption and ineffective charge separation, ultimately constraining device performance. The thickness of the absorber layer is equally significant, affecting the balance between light absorption and recombination. An excessively thin layer may fail to absorb adequate light, whereas an excessively thick layer heightens recombination losses, hence diminishing efficiency.[72]

Conversely, hole mobility demonstrated less influence on the model's predictions, ranking as the least significant of the assessed features. The findings underscore the pivotal influence of material characteristics, including defect density, thickness, and band gap, on the optimization of efficient APSCs. The results emphasize the necessity of concentrating on these factors during the optimization process, since they are

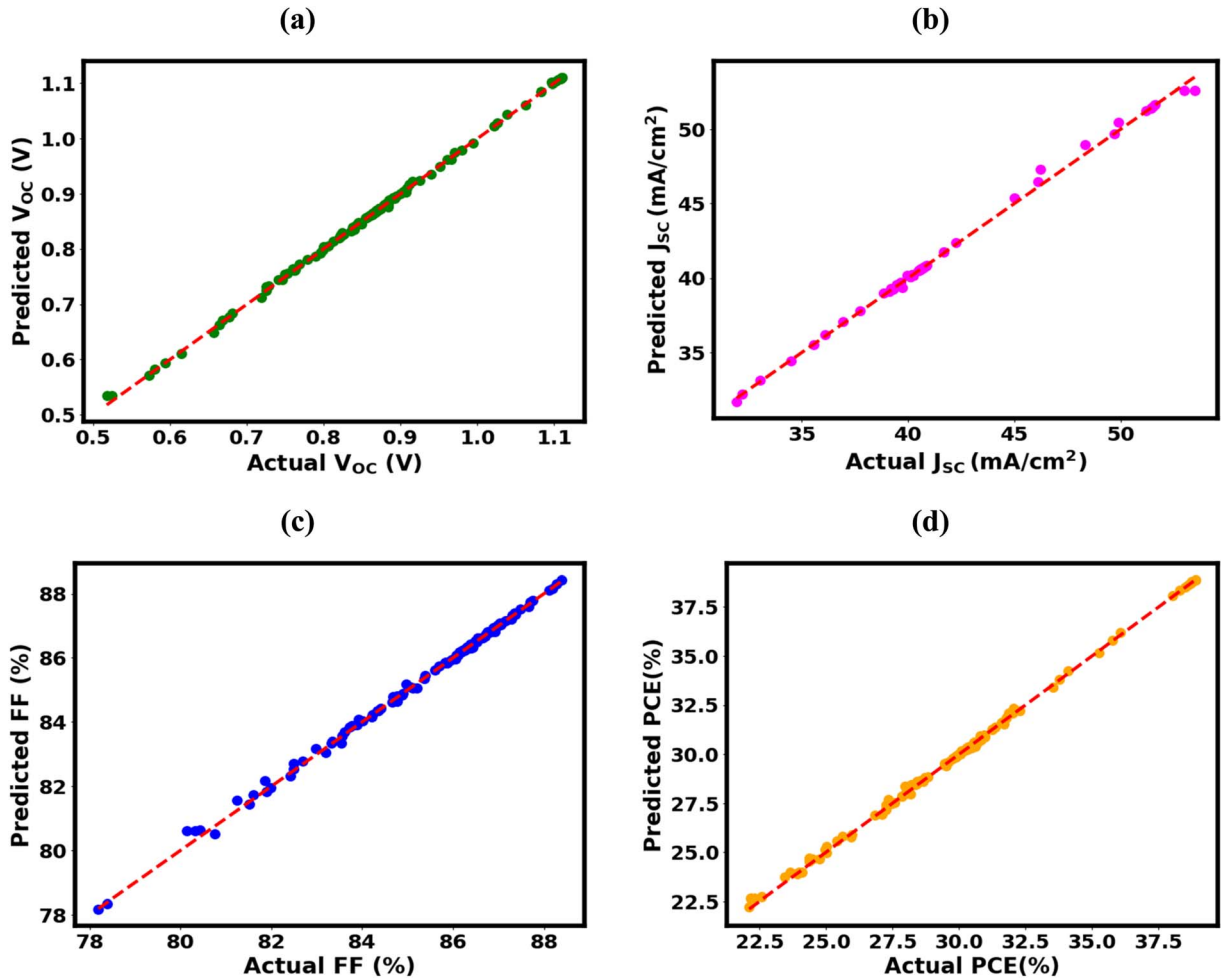

Fig. 18 Al/FTO/SnS_2/Sr_3BiI_3/CBTS/Ni cell performance evaluation: a ML comparison of predicted and actual results for (a) V_{OC}, (b) J_{SC}, (c) FF, and (d) PCE.

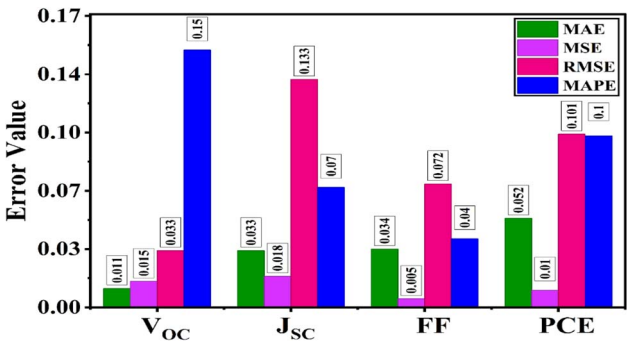

Fig. 19 Comparative assessment of error metrics for key PV parameters.

universally acknowledged as vital to device performance in anti-perovskite materials research. This examination of feature significance is essential for improving predictive models, facilitating a more focused strategy for material and device optimization, so augmenting both the precision and comprehensibility of machine learning-based solar cell design.

4.1.2. Shapley additive explanations (SHAP) analysis. This research evaluates the influence of individual features on the model's output through the SHAP plot, as demonstrated in Fig. 21. It offers a clear visualization of the physical parameters that significantly influence the target variable, serving as a valuable tool for model interpretation.[85,86] The *X*-axis illustrates SHAP values, which quantify the influence of each feature on the prediction, where positive values denote an enhancement and negative values signify a decrease. The *Y*-axis organizes input features according to their relative significance, offering a clear representation of their contributions. The defect density is the most critical factor, exerting a substantial negative impact on the model, indicating that increased defect density diminishes predicted performance.

Interface defects and band gap significantly influence the model, with increased values of these parameters resulting in reduced performance. This underscores the necessity of minimizing defects and optimizing the band gap. Conversely, attributes including thickness, electron mobility, dielectric permittivity, and hole mobility exhibit negligible influence on the model's output, as indicated by their SHAP values, which are

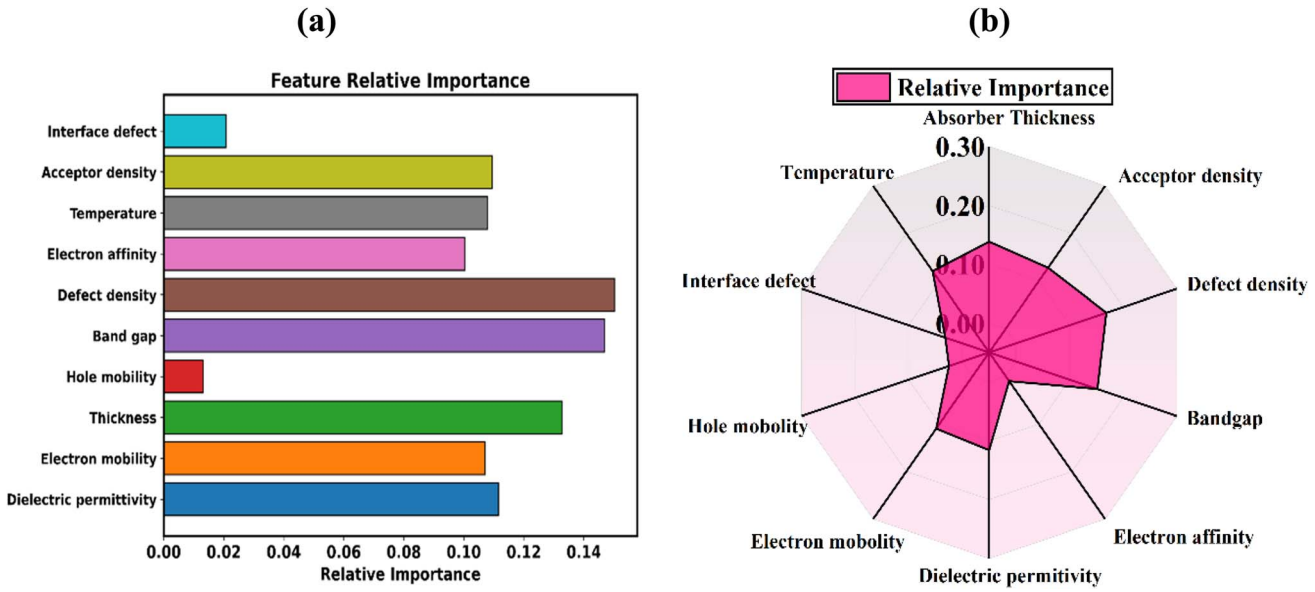

Fig. 20 (a) Bar and (b) radar chart representations of ML algorithm elucidate the relative significance of parameters influencing the efficiency of the Al/FTO/SnS_2/Sr_3BiI_3/CBTS/Ni device.

concentrated near zero. This indicates that although these parameters contribute to overall performance, their impact is less significant than that of defect-related features. SHAP analysis offers critical insights into the primary factors influencing photovoltaic performance, enabling researchers to prioritize material optimizations in the design and fabrication of more efficient solar cells. Minimizing defect density and optimizing the band gap can lead to substantial enhancements in performance and cost efficiency.

4.2. Model evaluation using ROC curve and confusion matrix

The Random Forest classification model was utilized to validate the SCAPS-1D simulation results and to offer new insights into the factors influencing the PV behavior of Sr_3BiI_3-based APSCs. The model's performance was assessed through the Receiver Operating Characteristic (ROC) curve and the confusion matrix, as shown in Fig. 22(a) and (b). The ROC curve demonstrated an area under the curve (AUC) value of 0.99215, indicating the model's outstanding capacity to differentiate between high- and low-efficiency solar cell categories. The pronounced curvature in the top-left corner signifies elevated sensitivity and specificity, accompanied by a minimal incidence of false classifications.

The confusion matrix (Fig. 22(b)) illustrates the model's precision, accurately identifying 132 true negatives (low-efficiency) and 66 true positives (high-efficiency), with no false positives and only two false negatives. The notable classification stability highlights the model's reliability and robustness in

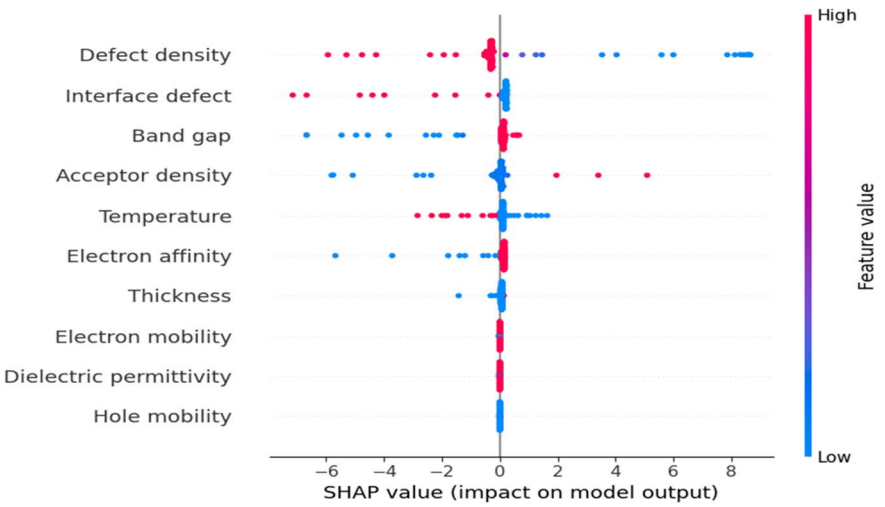

Fig. 21 Material property importance in model performance is derived from SHAP values.

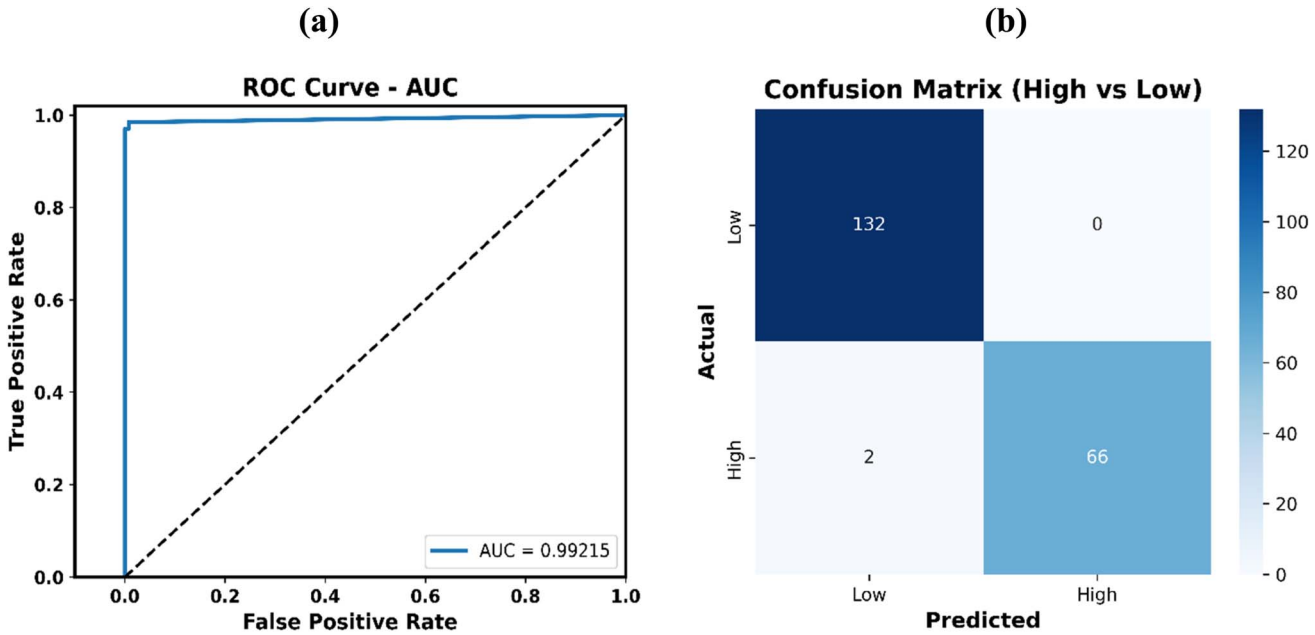

Fig. 22 Performance evaluation of the RF Model through (a) ROC curve and (b) confusion matrix.

forecasting solar cell performance. The RF model provides insights that are not immediately apparent, extending beyond the results obtained from SCAPS-1D, in addition to its classification accuracy. The internal feature evaluation process of the model identified defect density, absorber thickness, and ETL doping concentration as the key parameters affecting device efficiency. The RF model demonstrated non-linear and synergistic interactions among these parameters. Specifically, elevated ETL doping levels improve carrier extraction efficiency only when the HTL layer is adequately thin, whereas excessive absorber thickness reduces performance due to heightened recombination losses. The model also suggested a defect density threshold, below which additional reductions yield negligible performance improvements, indicating an inherent limitation of the material. The findings enhance the interpretive understanding of how structural and electronic parameters collectively influence device behavior, rather than simply confirming simulation results. The Random Forest model exhibits high predictive accuracy (AUC = 0.99215) and provides new insights into the interdependent relationships among material, structural, and electronic parameters influencing the photovoltaic efficiency of Sr_3BiI_3-based APSCs. This approach redefines machine learning from a verification tool to a predictive-diagnostic framework, informing future optimization strategies for high-performance, lead-free APSCs.

5. Conclusion

This research examines the optoelectronic properties and PV efficacy of Sr_3BiI_3-based APSCs utilizing DFT and SCAPS-1D simulation outcomes. The maximum PCE of 30.31% was attained using the Al/FTO/SnS_2/Sr_3BiI_3/CBTS/Ni configuration among four solar cell configurations. An in-depth examination of the features of the absorber and ETL indicated that the SnS_2-based ETL design displayed superior *J–V* characteristics, although both SnS_2 and IGZO ETLs showed enhanced quantum efficiency relative to other ETL configurations. The research examined the impact of total N_t at the ETL/absorber interface, revealing that the SnS_2-based ETL structure exhibited enhanced performance, whilst the PCBM-based ETL demonstrated the lowest PCE. The examination of the Nyquist plot yielded significant insights into the impedance and charge transfer characteristics of diverse ETL-based devices. The bigger semicircles in the WS_2 ETL design demonstrated elevated impedance and impeded charge transport, while the smaller semicircles in the PCBM ETL configuration exhibited diminished impedance and improved charge transport characteristics. The amalgamation of Random Forest machine learning and conventional simulation techniques enabled us to forecast solar cell performance with exceptional precision. The model predicted PCE with 98.9% accuracy, utilizing critical parameters including absorber thickness, defect density, and ETL characteristics. The findings offer significant insights into experimental fabrication, namely in optimizing ETL selection, defect density, and absorber layer properties to improve charge transport and minimize recombination losses. The integration of modeling and machine learning provides a robust foundation for expediting the advancement of efficient, lead-free antiperovskite solar cells and enhancing their economic feasibility in large-scale applications.

Ethical statement

All authors state that the manuscript does not involve humans, human data or tissue, or animals.

Author contributions

Bipul Chandra Biswas, Asadul Islam Shimul: simulation, resources, formal analysis, data curation, conceptualization, methodology, original manuscript writing, manuscript editing and revision, data acquisition, and validation. Karim Kriaa, Chemseddine Maatki, Noureddine Elboughdir, Md. Azizur Rahman: formal analysis, manuscript editing, and revision, data curation, supervision.

Conflicts of interest

The authors have no conflicts of interest.

Data availability

The data that support the findings of this study are available within the manuscript.

Funding statement

This work was supported and funded by the Deanship of Scientific Research at Imam Mohammad Ibn Saud Islamic University (IMSIU) (grant number IMSIU-DDRSP2502).

Acknowledgements

This work was supported and funded by the Deanship of Scientific Research at Imam Mohammad Ibn Saud Islamic University (IMSIU) (grant number IMSIU-DDRSP2502). The authors acknowledge that an artificial intelligence (AI) language model was utilized solely for grammatical refinement and enhancement of textual clarity. The authors confirm that all scientific concepts, data analyses, interpretations, and conclusions presented in this work are entirely their own and were not generated or influenced by the AI tool.

References

1 S. Gong, et al., A hot carrier perovskite solar cell with efficiency exceeding 27% enabled by ultrafast hot hole transfer with phthalocyanine derivatives, *Energy Environ. Sci.*, 2024, **17**(14), 5080–5090, DOI: **10.1039/D4EE01839G**.

2 D. Lan and M. A. Green, Combatting temperature and reverse-bias challenges facing perovskite solar cells, *Joule*, 2022, **6**(8), 1782–1797, DOI: **10.1016/j.joule.2022.06.014**.

3 S. S. Dipta and A. Uddin, Stability Issues of Perovskite Solar Cells: A Critical Review, *Energy Technol.*, 2021, **9**(11), 2100560, DOI: **10.1002/ente.202100560**.

4 M. Rahman, A. Lubaba, A. Irfan and Md. F. Rahman, New Double Perovskite Solar Cell Containing Ba_3 PCl_3 (A_3 BX_3) and $CsSnI_3$ (ABX_3) Leading to an Improved Efficiency Above 30%, *ChemistrySelect*, 2024, **9**(42), e202403217, DOI: **10.1002/slct.202403217**.

5 Md. S. Reza, A. Ghosh, N. Drissi, A. S. Mugdho, Md. S. Reza and M. M. Akter, In-Depth Analysis of Electron and Hole Transport Layers for Enhancing Ca_3 PI_3 Solar Cell Efficiency through Advanced Numerical Simulation, *Langmuir*, 2025, **41**(10), 6657–6674, DOI: **10.1021/acs.langmuir.4c04660**.

6 S. Ahmed, M. A. Gondal, A. S. Alzahrani, M. Parvaz, A. Ahmed and S. Hussain, Recent Trends and Challenges in Lead-Free Perovskite Solar Cells: A Critical Review, *ACS Appl. Energy Mater.*, 2024, **7**(4), 1382–1397, DOI: **10.1021/acsaem.3c02327**.

7 D. Jayan K and V. Sebastian, Comparative Study on the Performance of Different Lead-Based and Lead-Free Perovskite Solar Cells, *Adv. Theory Simul.*, 2021, **4**(5), 2100027, DOI: **10.1002/adts.202100027**.

8 L. Benahmedi, A. Besbes, R. Djelti and S. Moulebhar, DFT and SCAPS-1D simulation of single-layer and bilayer perovskite solar cells: Ca_3 BiI_3 and Sr_3 BiI_3, *Semicond. Sci. Technol.*, 2025, **40**(2), 025001, DOI: **10.1088/1361-6641/ada17e**.

9 A. Ghosh, et al., Investigating of novel inorganic cubic perovskites of A3BX3 (A=Ca, Sr, B P, As, X=I, Br) and their photovoltaic performance with efficiency over 28%, *J. Alloys Compd.*, 2024, **986**, 174097, DOI: **10.1016/j.jallcom.2024.174097**.

10 K. L. Schulte, et al., GaAs solar cells grown on acoustically spalled GaAs substrates with 27% efficiency, *Joule*, 2023, **7**(7), 1529–1542, DOI: **10.1016/j.joule.2023.05.019**.

11 M. K. Hossain, et al., Design and Simulation of Cs_2 $BiAgI_6$ Double Perovskite Solar Cells with Different Electron Transport Layers for Efficiency Enhancement, *Energy Fuels*, 2023, **37**(5), 3957–3979, DOI: **10.1021/acs.energyfuels.3c00181**.

12 A. S. M. Mosabbir, et al., Optimizing lead-free Cs_2 $AgBiBr_6$ double perovskite solar cells: insights from SCAPS and FDTD simulations, *Sustain. Energy Fuels*, 2024, **8**(18), 4311–4323, DOI: **10.1039/D4SE00958D**.

13 F. Ünlü, M. Deo, S. Mathur, T. Kirchartz and A. Kulkarni, Bismuth-based halide perovskite and perovskite-inspired light absorbing materials for photovoltaics, *J. Phys. Appl. Phys.*, 2022, **55**(11), 113002, DOI: **10.1088/1361-6463/ac3033**.

14 L. Zhang, K. Wang and B. Zou, Bismuth Halide Perovskite-Like Materials: Current Opportunities and Challenges, *ChemSusChem*, 2019, **12**(8), 1612–1630, DOI: **10.1002/cssc.201802930**.

15 L. C. Lee, T. N. Huq, J. L. MacManus-Driscoll and R. L. Z. Hoye, Research Update: Bismuth-based perovskite-inspired photovoltaic materials, *APL Mater.*, 2018, **6**(8), 084502, DOI: **10.1063/1.5029484**.

16 M.-C. Tang, et al., Bismuth-Based Perovskite-Inspired Solar Cells: In Situ Diagnostics Reveal Similarities and Differences in the Film Formation of Bismuth- and Lead-Based Films, *Sol. RRL*, 2019, **3**(7), 1800305, DOI: **10.1002/solr.201800305**.

17 Y. Liu, et al., All-inorganic Sn-based Perovskite Solar Cells: Status, Challenges, and Perspectives, *ChemSusChem*, 2020, **13**(24), 6477–6497, DOI: **10.1002/cssc.202001680**.

18 Y. Du, et al., Integration of Perovskite/Low-Dimensional Material Heterostructures for Optoelectronics and Artificial Visual Systems, *Adv. Funct. Mater.*, 2025, **35**(36), 2500953, DOI: **10.1002/adfm.202500953**.

19 S. Y. Leblebici, T. L. Chen, P. Olalde-Velasco, W. Yang and B. Ma, Reducing Exciton Binding Energy by Increasing Thin Film Permittivity: An Effective Approach To Enhance Exciton Separation Efficiency in Organic Solar Cells, *ACS Appl. Mater. Interfaces*, 2013, **5**(20), 10105–10110, DOI: 10.1021/am402744k.

20 Md. A. Rahman, et al., Impact of A-Cations Modified on the Structural, Electronic, Optical, Mechanical, and Solar Cell Performance of Inorganic Novel A_3 NCl_3 (A = Ba, Sr, and Ca) Perovskites, *Energy Fuels*, 2024, **38**(9), 8199–8217, DOI: 10.1021/acs.energyfuels.4c00525.

21 A. I. Shimul, A. Ghosh, S. R. Sarker and H. A. Alturaifi, Examining the contribution of charge transport layers to boost the performance over 26% in Sr_3 PCl_3 absorber-based bifacial perovskite solar cells, *RSC Adv.*, 2025, **15**(10), 7663–7681, DOI: 10.1039/D5RA00607D.

22 A. Ghosh, et al., Enhancing solar cell efficiency beyond 27% through the implementation of an efficient charge transport layer utilizing an innovative inorganic perovskite Sr3PI3, *J. Phys. Chem. Solids*, 2024, **190**, 112029, DOI: 10.1016/j.jpcs.2024.112029.

23 M. F. Rahman, et al., Exploring the impact of strain on the electronic and optical properties of inorganic novel cubic perovskite Sr_3 PI_3, *Phys. Scr.*, 2023, **98**(11), 115105, DOI: 10.1088/1402-4896/acfce9.

24 U. Farooq, et al., Surface Defects Passivation with Organic Salt for Highly Stable and Efficient Lead-Free Cs_3 Sb_2 I_9 Perovskite Solar Cells, *ACS Appl. Energy Mater.*, 2023, **6**(20), 10294–10302, DOI: 10.1021/acsaem.3c00983.

25 Z. Zhu, X. Jiang, D. Yu, N. Yu, Z. Ning and Q. Mi, Smooth and Compact $FASnI_3$ Films for Lead-Free Perovskite Solar Cells with over 14% Efficiency, *ACS Energy Lett.*, 2022, **7**(6), 2079–2083, DOI: 10.1021/acsenergylett.2c00776.

26 R. Sahani and S. K. Pandey, A Comparative Study of Different MASnI3-Based Perovskite Solar Cells to Identify an Optimized and Stable PSC Structure, *J. Electron. Mater.*, 2025, **54**(10), 8732–8744, DOI: 10.1007/s11664-025-12229-3.

27 F. Kherrat, et al., Performance enhancement of eco-friendly Cs3Sb2I9-based perovskite solar cell employing Nb2O5 and CuI as efficient charge transport layers, *Micro Nanostruct.*, 2023, **183**, 207676, DOI: 10.1016/j.micrna.2023.207676.

28 S. Jiao, T. Wang and Z. Zhou, Additive Engineering Toward Suppression of Sn^{2+} Oxidation in Sn–Pb Perovskite Solar Cells: Mechanisms, Advances, and Outlook, *ChemSusChem*, 2025, **18**(13), e202500333, DOI: 10.1002/cssc.202500333.

29 A. N. Khan, et al., Evaluating A2SrGeI6 (A = K and Rb) Lead-Free double Perovskites: Structural, Elastic, and optoelectronic insights for clean energy, *Inorg. Chem. Commun.*, 2025, **174**, 113949, DOI: 10.1016/j.inoche.2025.113949.

30 N. Bouri, T. A. Geleta, K. W. Guji, A. Hammad, S. Rabhi and K. Nouneh, Resistance dynamics in a solar cell with novel lead-free perovskite absorbers (LiMgI3 and NaMgI3): Performance optimization using SCAPS-1D simulation and impedance spectroscopy, *J. Phys. Chem. Solids*, 2025, **207**, 112972, DOI: 10.1016/j.jpcs.2025.112972.

31 J. D. Head and M. C. Zerner, A Broyden—Fletcher—Goldfarb—Shanno optimization procedure for molecular geometries, *Chem. Phys. Lett.*, 1985, **122**(3), 264–270, DOI: 10.1016/0009-2614(85)80574-1.

32 R. Gaillac, P. Pullumbi and F.-X. Coudert, ELATE: an open-source online application for analysis and visualization of elastic tensors, *J. Phys. Condens. Matter*, 2016, **28**(27), 275201, DOI: 10.1088/0953-8984/28/27/275201.

33 A. Saidarsan, S. Guruprasad, A. Malik, P. Basumatary and D. S. Ghosh, A critical review of unrealistic results in SCAPS-1D simulations: Causes, practical solutions and roadmap ahead, *Sol. Energy Mater. Sol. Cells*, 2025, **279**, 113230, DOI: 10.1016/j.solmat.2024.113230.

34 S. Rabhi, et al., Insight into $NaSiCl_3$: a lead-free perovskite for the next generation revealed by DFT and SCAPS-1D, *Phys. Chem. Chem. Phys.*, 2025, **27**(25), 13490–13507, DOI: 10.1039/D5CP01747E.

35 M. A. Benatallah, A. Elmohri, Y. I. Bouderbala, M. W. Alam and S. Rabhi, Boosting Efficiency in Flexible Perovskite Solar Cells with Novel HTLs and ETLs: A drift-diffusion numerical study of CBz-PAI Interlayers and MXene Back Contacts, *Adv. Theory Simul.*, 2025, **8**(5), 2401161, DOI: 10.1002/adts.202401161.

36 T. M. Khan, B. Islam and S. R. A. Ahmed, Performance analysis and optimization of SnSe thin-film solar cell with Cu2O HTL through a combination of SCAPS-1D and machine learning approaches, *Mater. Today Commun.*, 2024, **41**, 110490, DOI: 10.1016/j.mtcomm.2024.110490.

37 A. S. Mugdho, A. Ghosh, A. I. Shimul, H. A. Alturaifi and N. S. Awwad, Boosting the performances of Mg3SbBr3-Based perovskite solar cell with machine learning analysis over 27 % utilizing effective transport layers, *J. Phys. Chem. Solids*, 2025, **205**, 112828, DOI: 10.1016/j.jpcs.2025.112828.

38 T. Seyisi, et al., Major challenges for commercialization of perovskite solar cells: A critical review, *Energy Rep.*, 2025, **13**, 1400–1415, DOI: 10.1016/j.egyr.2025.01.019.

39 A. Hossain, H. AlMohamadi, B. Wang, Md. Akhtaruzzaman and M. M. Uddin, Structural, electronic, optical, mechanical, and thermal properties of A3MCl3 (A = Mg, Ca; M = N, Bi) halide perovskites: A first-principles study, *Comput. Condens. Matter*, 2025, **45**, e01116, DOI: 10.1016/j.cocom.2025.e01116.

40 N. Bouri, et al., Comparative study of solar cells based on triple and graded absorber layers with the compound CsSn1-xGexI3: Numerical study and optimization, *J. Phys. Chem. Solids*, 2025, **199**, 112561, DOI: 10.1016/j.jpcs.2025.112561.

41 S. Rabhi, L. Hafaifa, O. H. Alsalmi and A. S. Alali, Boosting bifacial efficiency in inverted perovskite solar cells: 95% bifaciality and 28% PCE through materials and device engineering, *New J. Chem.*, 2025, **49**(32), 13876–13887, DOI: 10.1039/D5NJ02604K.

42 A. Laassouli, M. Karouchi, A. Ejjabli, Y. Lachtioui and O. Bajjou, DFT study on K2AgSbI6: Exploring the electronic, optical, and elastic properties of a double perovskite, *Solid State Commun.*, 2025, **402**, 115947, DOI: 10.1016/j.ssc.2025.115947.

43 M. A. Hossain, M. R. Islam and M. M. Rana, Unveiling the promising physical properties of Ca3BiX3 (X = F, Cl, Br, and I) compounds: A comprehensive study on their suitability for high-performance optoelectronics, *Mater. Sci. Eng. B*, 2026, **323**, 118871, DOI: 10.1016/j.mseb.2025.118871.

44 M. K. Hossain, et al., Combined DFT, SCAPS-1D, and wxAMPS frameworks for design optimization of efficient Cs_2 $BiAgI_6$ -based perovskite solar cells with different charge transport layers, *RSC Adv.*, 2022, **12**(54), 34850–34873, DOI: 10.1039/D2RA06734J.

45 A. Ghosh, et al., Machine Learning-Driven SCAPS Modeling for Optimizing CH_3 NH_3 $SnBr_3$ Perovskite Solar Cells: Analytical Insights into Materials for Hole Transport and the Active Layer, *Langmuir*, 2025, **41**(17), 11215–11237, DOI: 10.1021/acs.langmuir.5c01125.

46 A. Ghosh, et al., Innovative double absorber solar cell design combining Ca3AsI3 and Ca3PI3 perovskites for achieving over 29% efficiency, *Opt. Laser Technol.*, 2025, **183**, 112399, DOI: 10.1016/j.optlastec.2024.112399.

47 Md. Shamim Reza, et al., Boosting the effectiveness of a cutting-edge Ca3NCl3 perovskite solar cell by fine-tuning the hole transport layer, *Mater. Sci. Eng. B*, 2024, **309**, 117656, DOI: 10.1016/j.mseb.2024.117656.

48 N. L. Dey, et al., Optimization of Sr3NCl3-based perovskite solar cell performance through the comparison of different electron and hole transport layers, *J. Phys. Chem. Solids*, 2025, **196**, 112386, DOI: 10.1016/j.jpcs.2024.112386.

49 X. Su, et al., Influence of lattice mismatch of nano-holed substrate on the crystallization of Lennard-Jones liquids, *J. Mol. Liq.*, 2025, **430**, 127673, DOI: 10.1016/j.molliq.2025.127673.

50 M. Aliaghayee, Optimization of the Perovskite Solar Cell Design with Layer Thickness Engineering for Improving the Photovoltaic Response Using SCAPS-1D, *J. Electron. Mater.*, 2023, **52**(4), 2475–2491, DOI: 10.1007/s11664-022-10203-x.

51 A. Mortadi, E. El Hafidi, M. Monkade and R. El Moznine, Investigating the influence of absorber layer thickness on the performance of perovskite solar cells: A combined simulation and impedance spectroscopy study, *Mater. Sci. Energy Technol.*, 2024, **7**, 158–165, DOI: 10.1016/j.mset.2023.10.001.

52 S. Tariq Jan and M. Noman, Influence of layer thickness, defect density, doping concentration, interface defects, work function, working temperature and reflecting coating on lead-free perovskite solar cell, *Sol. Energy*, 2022, **237**, 29–43, DOI: 10.1016/j.solener.2022.03.069.

53 K. Deepthi Jayan and V. Sebastian, Comprehensive device modelling and performance analysis of MASnI3 based perovskite solar cells with diverse ETM, HTM and back metal contacts, *Sol. Energy*, 2021, **217**, 40–48, DOI: 10.1016/j.solener.2021.01.058.

54 T. Zhang, Q. He, J. Yu, A. Chen, Z. Zhang and J. Pan, Recent progress in improving strategies of inorganic electron transport layers for perovskite solar cells, *Nano Energy*, 2022, **104**, 107918, DOI: 10.1016/j.nanoen.2022.107918.

55 T. Nakamura, W. Yanwachirakul, M. Imaizumi, M. Sugiyama, H. Akiyama and Y. Okada, Reducing Shockley–Read–Hall recombination losses in the depletion region of a solar cell by using a wide-gap emitter layer, *J. Appl. Phys.*, 2021, **130**(15), 153102, DOI: 10.1063/5.0060158.

56 Md. M. Haque, et al., Study on the interface defects of eco-friendly perovskite solar cells, *Sol. Energy*, 2022, **247**, 96–108, DOI: 10.1016/j.solener.2022.10.024.

57 F. Izadi, A. Ghobadi, A. Gharaati, M. Minbashi and A. Hajjiah, Effect of interface defects on high efficient perovskite solar cells, *Optik*, 2021, **227**, 166061, DOI: 10.1016/j.ijleo.2020.166061.

58 Q. Meng, et al., Effect of temperature on the performance of perovskite solar cells, *J. Mater. Sci. Mater. Electron.*, 2021, **32**(10), 12784–12792, DOI: 10.1007/s10854-020-03029-y.

59 T. Moot, et al., Temperature Coefficients of Perovskite Photovoltaics for Energy Yield Calculations, *ACS Energy Lett.*, 2021, **6**(5), 2038–2047, DOI: 10.1021/acsenergylett.1c00748.

60 J. R. Sofia and K. S. Joseph Wilson, Numerical StudiesOn Cs2AgBiCl6 Based All-Inorganic Perovskite Solar Cell Using SCAPS 1D, *J. Opt.*, 2025, DOI: 10.1007/s12596-025-02816-2.

61 L. Hao, et al., A tin-based perovskite solar cell with an inverted hole-free transport layer to achieve high energy conversion efficiency by SCAPS device simulation, *Opt. Quant. Electron.*, 2021, **53**(9), 524, DOI: 10.1007/s11082-021-03175-5.

62 N. J. Jeon, et al., Compositional engineering of perovskite materials for high-performance solar cells, *Nature*, 2015, **517**(7535), 476–480, DOI: 10.1038/nature14133.

63 Z. Jiang, et al., Reducing trap densities of perovskite films by the addition of hypoxanthine for high-performance and stable perovskite solar cells, *Chem. Eng. J.*, 2022, **436**, 135269, DOI: 10.1016/j.cej.2022.135269.

64 P. Calado, et al., Evidence for ion migration in hybrid perovskite solar cells with minimal hysteresis, *Nat. Commun.*, 2016, **7**(1), 13831, DOI: 10.1038/ncomms13831.

65 G. Richardson, et al., Can slow-moving ions explain hysteresis in the current–voltage curves of perovskite solar cells?, *Energy Environ. Sci.*, 2016, **9**(4), 1476–1485, DOI: 10.1039/C5EE02740C.

66 P. Caprioglio, et al., Open-circuit and short-circuit loss management in wide-gap perovskite p-i-n solar cells, *Nat. Commun.*, 2023, **14**(1), 932, DOI: 10.1038/s41467-023-36141-8.

67 W. Bulowski, et al., Optimization of the ETL titanium dioxide layer for inorganic perovskite solar cells, *J. Mater. Sci.*, 2024, **59**(17), 7283–7298, DOI: 10.1007/s10853-024-09581-w.

68 C. Chen, et al., 6.5% Certified Efficiency Sb_2 Se_3 Solar Cells Using PbS Colloidal Quantum Dot Film as Hole-Transporting Layer, *ACS Energy Lett.*, 2017, **2**(9), 2125–2132, DOI: 10.1021/acsenergylett.7b00648.

69 F. Li, et al., Perovskite Quantum Dot Solar Cells with 15.6% Efficiency and Improved Stability Enabled by an α-$CsPbI_3$/$FAPbI_3$ Bilayer Structure, *ACS Energy Lett.*, 2019, **4**(11), 2571–2578, DOI: 10.1021/acsenergylett.9b01920.

70 Md. M. Islam, Md. F. Rahman, Md. H. Rahman, M. Z. Bani-Fwaz, R. Pandey and Md. Harun-Or-Rashid, Unlocking the lead-free new all inorganic cubic halide perovskites of Ba3MI3 (M = P, As, Sb) with efficiency above 29%, *J. Mater. Sci.*, 2024, **59**(48), 22109–22131, DOI: **10.1007/s10853-024-10487-w**.

71 Md. A. I. Islam, Md. F. Rahman, Md. M. Islam, M. K. A. Mohammed and A. Irfan, Investigation of novel all-inorganic perovskites Ba_3 PX_3 (X = F, Cl, Br, I) with efficiency above 29%, *Phys. Chem. Chem. Phys.*, 2025, **27**(4), 1861–1883, DOI: **10.1039/D4CP04276J**.

72 Md. H. Rahman, et al., Comprehensive analysis of Sr3PCl3 absorber for solar cells using DFT, SCAPS-1D, and machine learning techniques, *Polyhedron*, 2025, **280**, 117676, DOI: **10.1016/j.poly.2025.117676**.

73 M. K. Hossain, et al., Exploring the Optoelectronic and Photovoltaic Characteristics of Lead-Free Cs_2 $TiBr_6$ Double Perovskite Solar Cells: A DFT and SCAPS-1D Investigations, *Adv. Electron. Mater.*, 2025, **11**(2), 2400348, DOI: **10.1002/aelm.202400348**.

74 B. K. Ravidas, M. K. Roy and D. P. Samajdar, Investigation of photovoltaic performance of lead-free CsSnI3-based perovskite solar cell with different hole transport layers: First Principle Calculations and SCAPS-1D Analysis, *Sol. Energy*, 2023, **249**, 163–173, DOI: **10.1016/j.solener.2022.11.025**.

75 N. Shrivastav, J. Madan and R. Pandey, Predicting photovoltaic efficiency in Cs-based perovskite solar cells: A comprehensive study integrating SCAPS simulation and machine learning models, *Solid State Commun.*, 2024, **380**, 115437, DOI: **10.1016/j.ssc.2024.115437**.

76 A. Ghosh, et al., Enhancement of sulfide-based absorber and charge transport layer solar cell performance using machine learning and the SCAPS-1D simulator, *Phys. Chem. Chem. Phys.*, 2025, **27**(29), 15645–15668, DOI: **10.1039/D5CP01664A**.

77 N. Kaur, R. Pandey, M. Khalid Hossain and J. Madan, Machine learning-aided optimization for transport layer parameters of low lead inorganic Zn-based mixed-halide perovskite solar cell, *Sol. Energy*, 2023, **264**, 112055, DOI: **10.1016/j.solener.2023.112055**.

78 D. T. Mihailović, et al., Analysis of Solar Irradiation Time Series Complexity and Predictability by Combining Kolmogorov Measures and Hamming Distance for La Reunion (France), *Entropy*, 2018, **20**(8), 570, DOI: **10.3390/e20080570**.

79 R. Kundara and S. Baghel, Predictive design of KSnI3-based perovskite solar cells using SCAPS and machine learning model, *Mater. Sci. Eng. B*, 2024, **307**, 117536, DOI: **10.1016/j.mseb.2024.117536**.

80 N. Shrivastav, et al., Advanced Computational Techniques for Optimizing Manganese-Based Perovskite Solar Cells: From SCAPS-1D Simulations to Machine Learning Predictions, *J. Electron. Mater.*, 2025, **54**(2), 1209–1217, DOI: **10.1007/s11664-024-11638-0**.

81 M. Hasanzadeh Azar, et al., SCAPS Empowered Machine Learning Modelling of Perovskite Solar Cells: Predictive Design of Active Layer and Hole Transport Materials, *Photonics*, 2023, **10**(3), 271, DOI: **10.3390/photonics10030271**.

82 N. A. Tukadiya, Z. D. Ponkiya, N. Joshi, D. Upadhyay and P. K. Jha, Machine learning and SCAPS-1D based prediction and validation of RbGeBr 3 perovskite solar cell, *Sol. Energy*, 2025, **300**, 113760, DOI: **10.1016/j.solener.2025.113760**.

83 T. M. Khan and S. R. A. Ahmed, Investigating the Performance of $FASnI_3$ -Based Perovskite Solar Cells with Various Electron and Hole Transport Layers: Machine Learning Approach and SCAPS-1D Analysis, *Adv. Theory Simul.*, 2024, **7**(10), 2400353, DOI: **10.1002/adts.202400353**.

84 N. Elboughdiri, et al., Innovative computational framework for Sr_3 $SbCl_3$ absorber optimization: DFT, SCAPS-1D, and machine learning perspectives, *New J. Chem.*, 2025, **49**(33), 14529–14552, DOI: **10.1039/D5NJ01823D**.

85 H. A. Jame, et al., Supervised Machine Learning-Aided SCAPS-Based Quantitative Analysis for the Discovery of Optimum Bromine Doping in Methylammonium Tin-Based Perovskite ($MASnI_{3-x}Br_x$), *ACS Appl. Mater. Interfaces*, 2022, **14**(1), 502–516, DOI: **10.1021/acsami.1c15030**.

86 V. Deswal and S. Baghel, Designing and optimization of a highly efficient and new lead-free Cs_2RbGaI_6 based double perovskite solar cell through SCAPS-1D and machine learning, *Inorg. Chem. Commun.*, 2025, **176**, 114316, DOI: **10.1016/j.inoche.2025.114316**.